



Towards an Understanding of the Challenges in Laser Beam Welding of Copper – Observation of the Laser-Matter Interaction Zone in Laser Beam Welding of Copper and Steel Using in Situ Synchrotron X-Ray Imaging

Florian Kaufmann¹ · Julian Schrauder¹ · Marc Hummel^{2,3} · Christoph Spurk² · Alexander Olowinsky³ · Felix Beckmann⁴ · Julian Moosmann⁴ · Stephan Roth^{1,5} · Michael Schmidt^{1,5,6}

Accepted: 28 August 2023 / Published online: 13 September 2023
© The Author(s) 2023

Abstract

The increasing demand for contacting applications in electric components such as batteries, power electronics and electric drives is boosting the use of laser-based copper processing. Laser beam welding is a key for an efficient and high-quality electric vehicle production due to its local, non-contact energy input and high automation capability enabling reproducible weld quality. Nevertheless, a major challenge in process design is the combination of energy-efficiency and precise process guidance with regard to weld seam depth and defect prevention (i.e. spatter, melt ejections), partly caused by the high thermal conductivity of copper. High power lasers in the near infrared range and emerging visible laser beam sources with excellent beam quality can provide a suitable joining solution for this purpose. However, the underlying physical phenomena are currently only partly understood and a reflection on the challenges of laser beam welding of copper compared to well researched steel processing has not yet been carried out. In order to improve the understanding of the effect of the different material properties and the influence of process parameters on the vapor capillary and melt pool geometry in laser beam welding, in situ synchrotron investigations on Cu-ETP and S235 using 515 and 1030 nm laser sources were conducted. The material phase contrast analysis was successfully used to distinguish vapor capillary and melt pool phase boundaries during the welding process with high spatial and temporal resolution up to 5 kHz. A significantly different vapor capillary geometry and sensitivity to parameter variation were found between the steel and copper material. In addition, the visualization of characteristic melt flows revealed different melt pool dynamics and a pronounced eddy close to the melt pool surface for copper, which is assumed to be causal for the observation of pronounced spatter formation during copper welding in a certain process window.

Keywords X-ray phase contrast observation · Copper · Keyhole welding · Electromobility · Process observation

Introduction

Climate change and environmental devastation are existential threats to Europe and the world, which is why the European Green Deal aims to transform Europe into a modern, resource-efficient, and competitive economy. For achieving sustainability of the internal combustion engine dominated transport sector, this implies a target reduction of 50% in net greenhouse gas emissions for cars and trucks by 2030 [1]. To achieve these goals, the market segment of zero-emission and low-emission vehicles in particular must be developed in order to enable a more environmentally friendly and smarter mobility.

The production of batteries, power electronics and electric motors plays an essential role in the efficient and high-quality production of this vehicles. As an analysis by the VMDA shows, the market for battery production equipment is growing constantly, forecasting a market volume of € 20 billion on global investment in lithium-ion battery production machinery in 2023. For these large-scale productions, reliable manufacturing technologies are needed, whereby the laser is an important solution provider for material processing, especially for joining applications [2].

Because of its local, non-contact energy input and the high automatability of laser beam welding processes, the technology offers great potential for the increased amount of joints of metallic materials compared to the drivetrain of internal combustion engines [3]. In addition, laser beam welding offers flexibility in the design of the joining area, which may be required considering the disruptive nature of current developments in battery production [4].

A comparison of the joined materials between conventional combustion technology and electrified/ electric powertrains reveals a shift from steels to an increasing use of copper materials for power transmission. While strength and geometry requirements or challenges resulting from highly corrosive environment like in the exhaust system, e.g. in throttle valves, were the main focus of conventional drivetrains, electrified drives add weld seam requirements like current carrying capacity, heat transfer capability or leak tightness specifications [5]. This is accompanied by a diversification of material thicknesses, required weld seam depths (ranging from μm -thin foils for example for arrester tab welding [6] to mm-thick copper hairpins [7] or busbars) and the number of welds per assembly.

A simple transfer of the well-researched laser beam welding process using brilliant beam sources in the near-infrared (NIR) wavelength range from steels to copper materials does not meet the aforementioned requirements: Investigations of the welding process of copper with NIR laser radiation report a lack of reproducibility and the occurrence of weld seam defects like pores, enhanced spatter formation, and irregular weld seam depth [8]. The reason for the small process window is seen in the material-specific physical properties of copper [9]. Improvements are observed through the use of currently intensively investigated approaches of changing the processing wavelength [10], the modification of the local and temporal energy input

[11], as well as the surface reflectance reduction through laser-based pre-processes [12].

However, to optimize the laser beam welding process of copper in combination with energy-efficiency and precise process guidance with regard to weld seam depth and defect prevention, the changes in the underlying physical phenomena when changing material from steel to copper and applying visible laser radiation need to be better understood.

In this work, the effect of different material-specific physical properties and the influence of process parameters on the vapor capillary and melt pool geometry during laser beam welding are studied through in situ synchrotron X-ray imaging investigations on Cu-ETP and S235 using 515 and 1030 nm disc lasers. In this way, the phase boundaries of vapor capillary and melt pool can be observed with high spatial and temporal resolution during the welding process and their dynamic behaviour can be analyzed. The aim is to identify the challenges and changes in laser beam welding of copper in order to improve the final weld quality by addressing the observed aspects in the design of the welding process. This should enable a more efficient and controllable joining process.

State of the Art

Material-Specific Physical Properties of Steel and Copper

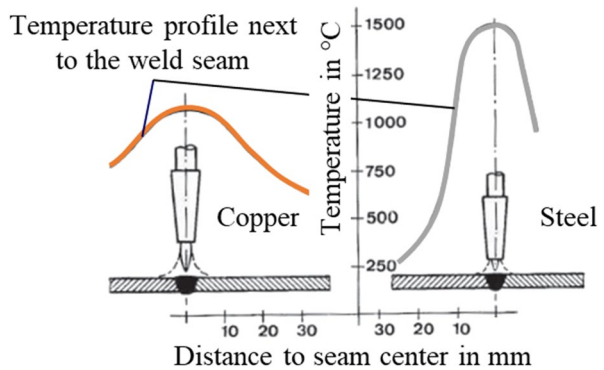
Selected physical properties of steel and copper are listed in Table 1. Apart from a higher density, the temperature range between melting and evaporation temperature is 275 K wider for copper. Because of its high electrical conductivity, which is about one power of ten higher than that of steel at room temperature, copper is well suited as a conductor of electricity.

As the material property of high electrical conductivity is associated with high thermal conductivity (Wiedemann-Franz rule [14]), the material poses a major challenge in a welding process. The thermal conductivity of copper at room temperature is about 8 times higher compared to steel and this ratio increases at elevated temperatures, as the decrease for copper over increasing temperature is lower [15]. Figure 1 illustrates the impact on the interaction zone for a heat conduction limited welding process, indicating a lower temperature gradient from the melting temperature in the weld seam to the surrounding base material for copper compared to steel.

Table 1 Physical properties of steel and copper [13]

Parameter	Unit	Steel	Copper
Density ρ	kg / m ³	7850	8935
Melting temperature T_m	°C	1471	1084
Evaporation temperature T_v	°C	2672	2560
Thermal conductivity λ_{th} (T=20 °C)	W / m*K	45	394
Electrical conductivity σ (T=20 °C)	1/ Ω *m ⁻¹	9,9*10 ⁶	5,9*10 ⁷

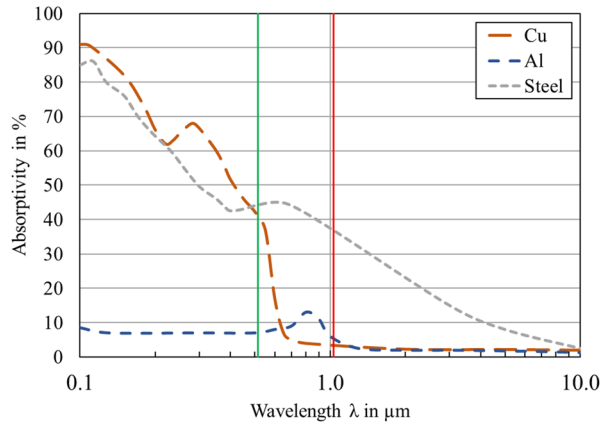
Fig. 1 Temperature curves when welding steel and copper based on [16]



In the case of copper, the energy is dissipated to a greater extent into the base material, which is thus no longer available for melting. So to generate and maintain a stable welding process, a concentrated heat input must be applied or a pre-heating of the component has to be carried out [16]. In addition, this conduction leads to a more size- and geometry-dependent processing window in copper welding [17]. Engler observes a significant dependence of the weld seam width on the feed rate for laser beam welding of stainless steel, which significantly increases with decreasing feed rate at constant penetration depth. This correlation can be explained by the low thermal conductivity of the material, leading to an increased heat accumulation in the interaction zone using slow feed rates due to the higher line energy. For copper on the other hand, no dependence was found [9]. As copper is often used as a pure material (Cu-ETP, Cu-OF) [18], it is characterised by a melting point, in contrast to steels which, due to the alloying of various elements, have a melting interval leading to abrupt liquefaction and solidification of the non-ferrous metal. In combination with a lower surface tension [15], dynamic effects in the interaction zone are thereby promoted: Due to the lower surface tension, the counteracting forces for spatter detachment according to existing spatter formation models [19] decrease and the self-damping of the dynamics, induced by the time-varying energy input in the interaction zone, is reduced. Thermal expansion, which is increased by a factor of 1.4 [20], and about twice as much structure-related shrinkage occurring during solidification compared to steels additionally impedes the design of the welding process due to induced large deformations and resulting stresses [16].

Beside the aforementioned factors, a major issue in laser beam welding of copper is the high reflection at room temperature. Especially when using infrared wavelengths, the current industrial standard, high intensities are required to initiate a deep penetration welding process [21]. Depending on the wavelength, the absorption of copper is less than 5% at room temperature. Starting from a wavelength of about 700 nm the absorption however rises significantly with declining wavelength, as indicated in Fig. 2. The plot shows absorptivity behavior of copper, aluminum, and steel, calculated from the reflectivity [3] with measured data for the refractive index n and the absorption index k from [22].

Fig. 2 Absorptivity for Cu, Al, and steel at room temperature



Moreover, it is assumed that the low absorptivity causes the observed high sensitivity of the laser welding process of copper to variations in surface conditions such as oxidation or roughness [23]. As the absorptivity for infrared radiation significantly rises at the phase transition from solid to liquid, the welding process is of a rather unstable nature between low and almost full energy coupling [8]. Comparing absorptivity values for copper and steel reveals a factor of 10 between both materials for perpendicular beam incidence at room temperature. In addition, the absorptivity of steel compared to copper for infrared radiation shows less temperature dependence and a reduced dependence on the processing wavelength is observed. It is also interesting to note that the absorptivity value of steel is close to that of copper for green laser radiation, where investigations have shown altered laser beam welding process behaviour compared to NIR laser radiation [24]. In sum, all of these factors make copper a difficult to process material for laser beam welding.

Laser Beam Welding and Analytical Model Representations

In general, two welding regimes are distinguished in the laser beam welding process: Heat conduction welding and deep penetration welding. An incident laser beam with a low power density heats the material locally. If a certain power density is exceeded, the melting point of the material is reached, and local melting on the material surface in the irradiated area takes place. By moving the laser beam or the material sample, a heat-conduction weld is formed [3]. Being characterised by single laser-matter interaction, this process regime can only generate limited penetration depths that do not exceed an aspect ratio (quotient of seam width and seam depth) of one. Consequently, it is primarily the heat conduction properties that are decisive for the weld seam characteristics (see [Material-Specific Physical Properties of Steel and Copper](#) section).

A further increase in power density causes the deep penetration threshold to be reached, i.e. the threshold at which the temperature of the melt pool on the sample surface is sufficient to transform material into a vaporous state. This evaporation leads to a deformation of the melt pool (induced by recoil pressure) and

consequently to increased reflections of the laser beam. A vapour capillary (key-hole) is formed, efficiently increasing the total absorption by multiple reflections inside [11]. The resulting aspect ratio can easily reach 10:1.

Theoretical considerations of the authors in [25] stated that the deep penetration threshold can be characterized using an analytic description with P/d values per material. These findings have been confirmed by [8] based on experimental investigations on steel and copper using infrared and green laser beam sources. Back reflections at the onset of the welding process, however, which persist until the deep welding process is fully developed, can damage optical elements or even the beam source itself [12]. This phase of process setup also reduces the effective joining length, especially noticeable for copper welding using NIR laser radiation, as it was found to be influenced by wavelength-dependent absorptivity [26].

Various dynamic and static model representations have been developed to analyze the relationships in the vapor capillary, the flow conditions in the melt pool or the entire laser beam welding process in deep penetration mode [27]. Beck for example developed a comprehensive model taking into account, the absorption of the laser radiation in the plasma, Fresnel absorption at the vapour capillary including multiple reflections, heat conduction, melt pool and metal vapour flow dynamics at low and high processing speeds, as well as wall shear stresses induced by the metal vapour flow [28]. Derived analytical approximations for a stationary laser beam welding process allow for a less complex analysis of influencing parameters, for example on the influence of different process parameters on the achievable penetration depth. Due to the high complexity of the dynamic relationships, however, these models are only capable of providing accurate results under simplified assumptions in limited parameter ranges.

Since a large part of the incident radiation is absorbed and reflected at the capillary front wall [29], its inclination and shape are of particular importance for the development of the deep penetration welding process. The formation of the vapour capillary geometry in 1 mm thick steel sheets is investigated by the authors in [30] mainly from the lateral displacement of the melt, starting from the capillary front wall. Based on this model representation, the vapour capillary geometry was investigated in several publications as a function of the process parameters welding speed, laser beam intensity and material properties. The comparison with experimental observations revealed findings about the inclination of the vapour capillary, the formation of spatter, and the resulting weld seam quality [31, 32].

Investigating the effect of higher feed rates on the welding process, the authors in [33] analyzed the capillary shape to determine the potential of feed rate increase in terms of process efficiency and the influence of the capillary geometry. Observing a strong correlation between the capillary geometry and the feed rate, a shape transition from a U-shape to a wedge shape for increased feed rate is detected with an aperture to the sample surface far higher than the applied beam diameter. The results further indicate that the absorptivity is related to the capillary geometry. As the thermal efficiency of the laser beam welding process is known to increase with increased feed rate [34], the feed rate should be chosen as high as the humping limit in order to achieve a high process efficiency. In laser beam welding of copper,

increased feed rates [35] as well as power modulation [36] have been observed to stabilize the welding process.

Process Observation Using in Situ X-Ray Imaging

The analysis and fundamental understanding of the geometry of the vapor capillary as well as the physical processes within are major research questions since the beginning of the process investigations on laser beam welding. Conclusions about the width, length, inclination, and shape of the vapor capillary have been derived experimentally mainly by metallurgical evaluation of the weld seam or by introducing contrasting materials with higher melting points than the base material into the melt pool [37]. Furthermore, camera-based observation techniques are widely used.

In comparison to visual and thermal imaging methods, in situ X-ray tomography enables a deeper investigation of laser-based processes in metals by a visualization of the phase boundaries. Since the damping of the X-ray photons penetrating a metal depends on the mass density of the irradiated material, which is lower in a gas-filled capillary than in the solid material ($Q_{\text{Gas}} < Q_{\text{Solid}} \approx Q_{\text{Liquid}}$), conclusions regarding the geometrical conditions of the laser-matter interaction zone can be drawn from the detection of the transmitted intensity [38]. Therefore, a scintillator for converting the attenuated X-ray into visible light and a conventional high-speed camera are typically used in the experimental setup [39].

Using a microfocus tube as an X-ray source at a 1 kHz acquisition rate, the effect of keyhole behavior on spatter and pore formation in copper welding was studied [40]. The authors in [41] investigated the highly dynamic behavior of the vapor capillary when processing copper with a multimode fiber laser. A comparison of the copper welding process using infrared and green laser radiation with identical optical setup revealed a lower feed rate sensitivity using 515 nm wavelength compared to 1030 nm wavelength. In addition, it was stated that multiple reflections have an increased effect in the case of infrared laser radiation, as the absorptivity for 1030 nm is lower compared to the wavelength of 515 nm, becoming particularly visible when investigating the capillary in width direction, where a decisive bulge was found in the lower keyhole area [26]. The authors in [42] performed porosity analysis in CuSn6 weld seams for same processing parameters for 515 and 1030 nm laser sources using in situ synchrotron observation. The green laser beam was observed to lead to a higher porosity, which is more evenly distributed over the entire capillary depth. It is assumed that this fact is related to the higher absorptivity of 515 nm compared to 1030 nm when impinging inside the vapor capillary.

As the pixels of the grey value pictures of the X-ray video contain information about the remaining effective thickness of the processed material, the authors in [43] developed a method for the three-dimensional reconstruction of the vapor capillary based on a calculated attenuation coefficient for each material. This reconstruction of the capillary can be used to investigate the locally absorbed irradiance as well as the total absorptivity in the interaction zone applying a ray tracing algorithm including the actual laser properties [33].

In addition, the use of tracer particles with a high melting point, e.g. tungsten powder, enables the observation of the fluid flows in the melt pool, whereby vortex areas, for example, become visible [44]. The authors in [45] investigate the influence of the focal position on the melt flow during laser beam welding of steel by means of evaluating the characteristic melt flow based on tracer particle trajectory analysis. A significant dependence of the capillary shape, the melt flow direction, and the melt pool geometry mainly in the upper half of the melt pool on the focal position was observed. In situ X-ray imaging therefore provides a viable method for the derivation of process knowledge on laser beam welding in the deep penetration regime, especially since the boundary conditions are closer to the real welding process compared to investigations carried out using a glass-metal sandwich setup [46] or capillary observations obtained from the welding of transparent media like water or ice [47].

In sum, the state of the art provides a broad knowledge of the factors influencing the process behavior of keyhole welding of copper and steel, together with suitable methods for in situ process observation. As the materials properties and process parameters are the key factors influencing the laser-metal interaction and melt pool geometry [48], the understanding and control over the underlying phenomena is essential to maximize efficiency and minimize defect susceptibility. In order to extend the fundamental process understanding on the effect of different physical properties of copper and steel material on the laser beam welding process and the challenges in copper processing, this study uses the capabilities of in situ high-speed synchrotron X-ray imaging in terms of the detailed visualization of the keyhole behavior and its interactions with the surrounding melt pool. The results analysed in the literature raise the following research questions for this work:

- How do the different physical properties of steel and copper affect the process zone shape and capillary geometry when applying 515 and 1030 nm laser radiation with equal beam diameter?
- How do the main process parameters (laser power P_L , feed rate v) influence the vapor capillary geometry?

Due to the fact that the capillary front wall is the first point of interaction between laser radiation and metal, which is of great importance for the formation of the welding process, it will be studied in detail. The material samples are analyzed by means of material phase contrast method to investigate the dynamic behavior of boundaries between solid, liquid, and gaseous material phases for Cu-ETP and S235JR mild steel.

Experimental Setup and Methods

In this section, the synchrotron X-ray welding setup and the experimental procedure are presented. Afterwards, applied methods for data processing and evaluation of the measurement results are introduced.

Fig. 3 Schematic sketch of the experimental setup for the conduction of in situ synchrotron investigations

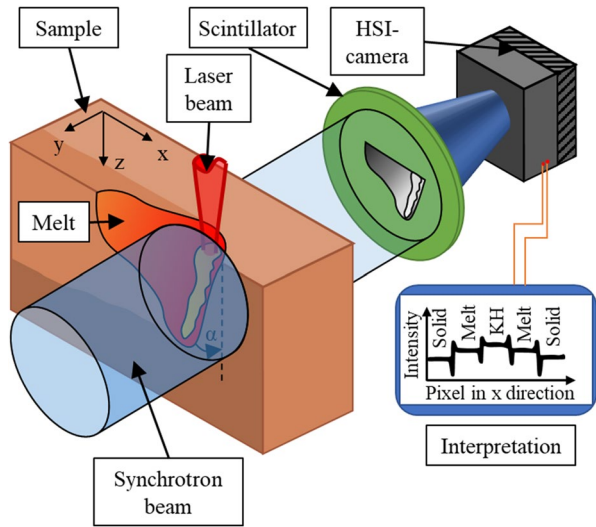


Table 2 Parameters and properties of the synchrotron imaging setup

Dimension	Unit	P07 Petra III
Operation mode	-	Low Beta
Photon energy	keV	89
Beam area	mm ²	2 × 2
Scintillator material	-	Ce:GAGG
Scintillator size	mm ²	11 × 11
Scintillator thickness	μm	1000
Distance	mm	3500

Synchrotron and Laser Beam Welding Setup

The HERION high-energy beamline P07 (EH4) of Petra III at the German Electron Synchrotron DESY in Hamburg, Germany [49], provided the basis for conducting the in situ synchrotron welding experiments. A customized experimental setup was installed, which is shown schematically in Fig. 3. The synchrotron beamline and imaging parameters are listed in Table 2.

The main elements of the X-ray imaging system are the DESY-synchrotron which provides the X-ray source (blue), a scintillator (green), and a high-speed camera (black). The synchrotron beam with an area of 2 × 2 mm² irradiates the moved sample with a dimension of 100 × 30 × 2 mm³, which is laser processed from the top side (laser beam propagation in z-direction). The laser and synchrotron beam are aligned perpendicular to each other in the region of interest. The penetrating X-ray photons are damped in the workpiece dependent on the mass density, which is lower for a gas-filled capillary compared to the solid sample. The transmitted, attenuated beam is converted into visible light using a Cer-doped GaGG:Ce (Gadolinium Aluminum

Gallium Garnet(Ce)) scintillator with a thickness of 1000 μm . The intrinsic glow of the scintillator screen stimulated by the X-rays was recorded from the back site with a high-speed camera (i-SPEED 727, iX Cameras) and a magnification lens. The videos were recorded at a resolution of 1536×2072 pixels with a frame rate of 5 kHz and an exposure time of 0.2 ms. This setup enables a spatial resolution of 396 pixels/mm with an evaluable area of about 2 mm in diameter. Considering the divergence of the X-ray beam is between 0.0018 mrad and 0.027 mrad [50], the influence of the penumbra on the observed blur is negligible.

For the presented investigations, the beamline was in Low Beta operation mode using a photon energy of 89 keV. The representation of the resulting X-ray images can be seen in the insert on the right-hand side of Fig. 3. It indicates material phase contrast in the interaction zone, characterized by different intensity levels and noticeable peaks at the transition [51]. The resulting image sequence is referred to as “X-ray video” in the following.

The laser beam welding setup consisted of two disc lasers, galvanometer scanning optics and a linear axis for applying the feed rate v . The parameters and properties of the laser beam sources and the optical setup used are given in Table 3.

A frequency-doubled disk laser emitting at a wavelength of $\lambda = 515$ nm and a disk laser emitting at $\lambda = 1030$ nm from the company Trumpf (TruDisk Pulse 421, TruDisk 8001, Trumpf GmbH, Ditzingen, Germany) were used within the welding experiments. The beam-delivery fibers coupled to the 2D-galvanometer scanners with appropriate coatings for each laser wavelength (Newson NV, Dendermonde, Belgium) had a core diameter of $d_{\text{LLK}} = 100$ μm . Using a collimation length of $f_{\text{C}} = 80$ mm and f-theta focusing optics with a focal length of $f_{\text{F}} = 163$ mm, a magnification ratio of 1:2 was obtained in each case. A spot diameter of $d_{\text{F}} = 222.5$ mm in almost top-hat intensity distribution was measured with a Primes Micro-SpotMonitor (Primes GmbH, Pfungstadt, Germany) for the green laser welding setup, and $d_{\text{F}} = 214.6$ mm for the infrared laser welding system respectively.

The metal specimens consisting of mild steel S235JR and Cu-ETP (CW004A) with a ground top surface were fixed in a motorized clamping device mounted on an electromagnetic high-speed x-y-axis stage (Jenny Science AG, Rain, Switzerland).

Table 3 Parameters and properties of the laser beam sources and the optical setups used in this investigation

Parameter	Unit	Trumpf TruDisk Pulse 421	Trumpf TruDisk 8001
Laser medium	-	Disc	Disc
Wavelength λ	nm	515	1030
Laser power P_{max}	W	400 cw / 4000 pulsed	8000 cw
Fiber diameter d_{LLK}	μm	100	100
Focal length collimator f_{C}	mm	80	80
Focal length F-Theta focusing optics f_{F}	mm	163	163
Focal diameter d_{F}	μm	222.5	214.6

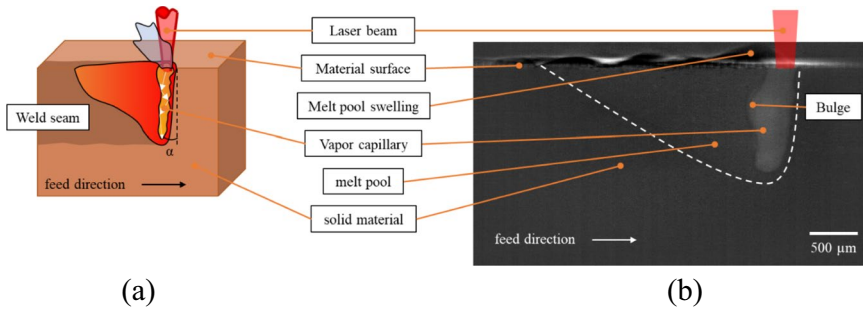


Fig. 4 **a** Schematic illustration of the interaction zone in deep penetration laser beam welding and **b** X-ray image of laser beam welding of Cu-ETP $t=2$ mm, $\lambda=1030$ nm, $d_F = 200$ μm , $P_L = 3500$ W, $v = 133$ mm/s

The maximum travel speed is limited to 2000 mm/s. The laser beam was aligned to the center of the specimen at $t/2$ for all side view experiments. The focal position was set on the workpiece top surface. In order to ensure the recording of the interaction zone during the whole experiment in side-view (x - z -plane), the sample was moved with feed rate v while the mirrors of the galvanometer scanners were set to zero position (intersection of the laser beam and the synchrotron beam while welding).

The schematic illustration of the interaction zone in deep penetration welding and a single image taken from an X-ray video of the copper welding process ($t=2$ mm, $\lambda=1030$ nm, $d_F = 200$ μm , $P_L = 3500$ W, $v = 133$ mm/s) are presented side by side in Fig. 4. Analyzing the extract of the irradiated area, the characteristic elements vapor capillary, melt pool, and the resolidified melt in the weld seam become visible.

Due to the reduced attenuation of the X-ray beam in the metal vapor-containing capillary, an increased gray value is detected on the camera sensor in that region. The shape of the melt pool is indicated by the white dashed line, separating the liquid phase from the base material in front of the capillary and from the solidified weld seam in the back (against feed direction). The associated melt pool dynamics can be recognized well from the melt pool swelling at the material surface, where melt flows around the capillary from different flow directions are meeting each other. In addition, capillary bulging, i.e. the rapid change in geometry, can be observed, which is assumed to be related to the time-dependent absorption of the irradiated laser power.

The process parameters investigated in the experimental campaign are listed in Table 4.

Partial penetration welds at a length of $l_{\text{Weld}} = 50$ mm with pulse length t_p selected respectively were generated using the NIR laser beam source. As the maximum energy per pulse of the TruDisk Pulse 421 is 40 J, the pulse duration was adjusted to the maximum possible value at a given laser power P_L . This allows comparable weld seams with limited length to be produced. Nitrogen was used for process zone coverage, supplied through a lateral nozzle against the welding direction for both

Table 4 Overview of the used process parameters for welding in partial penetration mode

Dimension	Unit	Choice of Parameters
Material of sample	-	S235JR, Cu-ETP
Feed rate v	mm/s	66.7; 100; 133.3; 200; 300, 500
Laser power P_L	W	500–4000
Energy of pulse (E)	J	40 = const. @ $\lambda = 515$ nm/ var. @ $\lambda = 1030$ nm
Pulse length (t_p)	ms	$40 \cdot P_L (\text{kW})^{-1}$ @ $\lambda = 515$ nm/ $3 \cdot v (\text{m/min})^{-1}$ @ $\lambda = 1030$ nm
Focal position z_{Fok}	mm	0 (top surface)
Shielding gas	-	N ₂ , 50 l/min
Frame rate X-ray ($f_{\text{X-ray}}$)	kHz	5 = const.

metals. To protect the welding optics from spatter and metal fume, a compressed air-fed cross jet was installed. The laser power was emitted in one single rectangular pulse of length t_p over the whole weld seam at constant feed rate up to $v = 500$ mm/s. Note that not the full parameter matrix consisting of laser power P_L , feed rate v , and wavelength λ was conducted for both materials: The welds were planned in order to achieve penetration depths that could be fully imaged on the camera sensor and resulted in comparable penetration depths or line energies in deep penetration welding regime.

Data Evaluation – Image Processing and Analysis of the Velocity Field of the Melt Pool

To ensure that the greyscale values result from local density variations in the metal and not from the intensity profile of the X-ray beam, a post-processing procedure was used, which is described in detail in our previous study [26]. Consisting of a subtraction of an averaged background image from the normalized X-ray videos, the phase contrast is further enhanced by Kalman filtering [52] and adjusting the color space of the images to facilitate the detection of image features [39]. This shading algorithm, applied to each individual image, reduces background noise and vignetting caused by the X-ray beam.

The capillary geometry was evaluation using the temporal average of the pixel values, taking into account all relevant images of the stationary welding process from the X-ray video. The capillary depth was determined as the distance from the surface of the material (see Fig. 4) perpendicular to the capillary tip (lowest point in z-direction) and its front wall inclination α was measured. By calculating the temporal standard deviation of each pixel according to Eq. (1), temporal variations within the X-ray videos can be identified, which highlight variations of the geometry of the capillary.

$$\sigma = \sqrt{\frac{1}{n} \sum_{i=1}^n (x_i - \bar{x})^2}, \quad (1)$$

Where x_i is the current pixel value at time i and \bar{x} is the average intensity value of the considered time interval. Thus, if sigma is large or there are bright pixels in the average intensity image, the individual image values at this position are scattered and widely distributed relative to the mean value.

In addition, tungsten particles were used to visualize the melt flow during laser beam welding. The tungsten particles were inserted in drilled holes with a diameter of $d_{\text{Drilling}} = 300 \mu\text{m}$ on the top surface of the sample, which was subsequently welded. The particles are characterized by a mean diameter of $d = 60 \mu\text{m}$, the distance between two consecutive holes in welding direction measures 10 mm. The particle movement was recorded at a frame rate of 5 kHz during the welding process. A comparable procedure is reported in [45], introducing tungsten carbide tracer particles into the weld. Since the authors and investigations in [53] do not observe significant differences in the velocity distribution for different particle sizes, it is assumed that there is only a negligible influence of the size of the tracer particles on the measured melt flow. By tracking the particle movement in side-view (projected onto the x - z plane) using synchrotron X-ray imaging from frame to frame until the particle solidifies in the weld seam (qualitatively determinable from the point at which a single particle's movement becomes a uniform displacement against welding direction at the same feed rate as the workpiece), the visualization of the melt flow in the interaction zone becomes possible. To facilitate a statistically relevant analysis of the characteristic melt flow, an algorithm based on the method described in [45] was applied, involving averaging over multiple tracer particle trajectories. The workflow is illustrated in Fig. 5.

The tungsten particles can be clearly identified as numerous black marks in the melt pool of the post-processed X-ray video (Introduction section). Numerous individual particles were successively tracked frame by frame, resulting in at least 30 trajectories per parameter set (see State of the Art section). Afterwards, each particle's continuous trajectory was interpolated from the measured positions recorded at equidistant imaging times using a cubic spline function [53]. This procedure ensures that the calculated trajectory passes through all detected positions with minimum acceleration of the tracer particle [54]. The interpolated particle trajectories are then evaluated in terms of their time- and position-dependent velocity and acceleration components (Experimental Setup and Methods section). Finally, an averaged melt pool velocity distribution was calculated by averaging over trajectories identified at different times during the laser beam welding process. A smoothing of the calculated flow distribution was performed by the inclusion of nine equidistantly interpolated

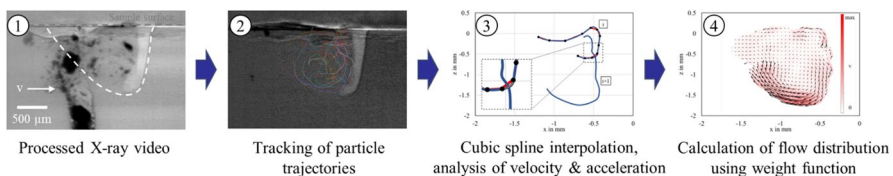


Fig. 5 Schematic illustration of the workflow for the calculation of the characteristic melt flow during laser beam welding from tracer particle trajectories

points between two measured positions. The averaged melt flow velocity was calculated near the nodes of an equidistant x-z-meshgrid with a spacing of 2.5 μm . For every node, the vectorial velocities at their positions were averaged according to the equations of Ref. [45] using the weight function, taking into account only the points on spline curves located within a radius closer than 0.1 mm around the actual node. An example result indicating flow directions and color-coded velocity regions can be seen in “Results and Discussion” section of Fig. 5.

Results and Discussion

Vapor Capillary Geometry of Steel and Copper Using 1030 nm Processing Wavelength

Figures 6 and 7 show the evolution of the vapor capillary geometry for laser beam welding of steel and copper for laser power $P_L = 0.5$ kW and 1 kW and feed rate v from 66.7 mm/s to 300 mm/s using 1030 nm laser radiation. For copper the laser power needs to be increased as the deep penetration threshold for NIR laser radiation was observed experimentally at 12.500 W/mm [24] and comparable penetration depths are of interest.

To evaluate the dynamic behavior, images of the standard deviation are given in addition to the temporal averaged X-ray images. If the capillary geometry and the development versus process parameters are compared for both materials, clear differences become apparent. For S235JR, the capillary shape at low feed rate ($v=66.7$ mm/s) is characterized by an almost I-shape (see orange illustration). As the feed rate is increased, the aperture at the sample surface increases and the average shape becomes similar to a V-shape with a bulge at the back wall in the lower part of the capillary. As a result, the reflection losses of the irradiated energy increase [28]. In line, the penetration depth into the material decreases with increasing feed rate, illustrated through Δe , which corresponds to the first finding. The third observed geometry variation is a significant increase of the capillary front wall angle α , if the sample is moved faster through the laser beam. If the laser power is increased, the penetration depth increases, which is associated with a more upright capillary for all feed rates investigated. The capillary is drilled more in laser beam direction as the power is increased, generating a higher recoil pressure on its front wall.

The plotting of the standard deviation for steel reveals a limited dynamic rim of the capillary at low feed rates, which increases significantly as the feed rate and the laser power are increased. This becomes particularly evident when looking at the back wall for $P_L = 1$ kW, $v=200$ mm/s, and $v=300$ mm/s respectively, where an enlarged white area is noticeable, indicating a varying energy coupling in that region. Theoretical assumptions in [55] and experimental investigations in [55] confirmed that the effects of the reflected laser radiation on the capillary back wall are more pronounced as the inclination of the capillary front increases.

In general, the vapour capillary geometry of copper using 1030 nm laser radiation shows a more bulbous shape for the investigated parameter range. The widest

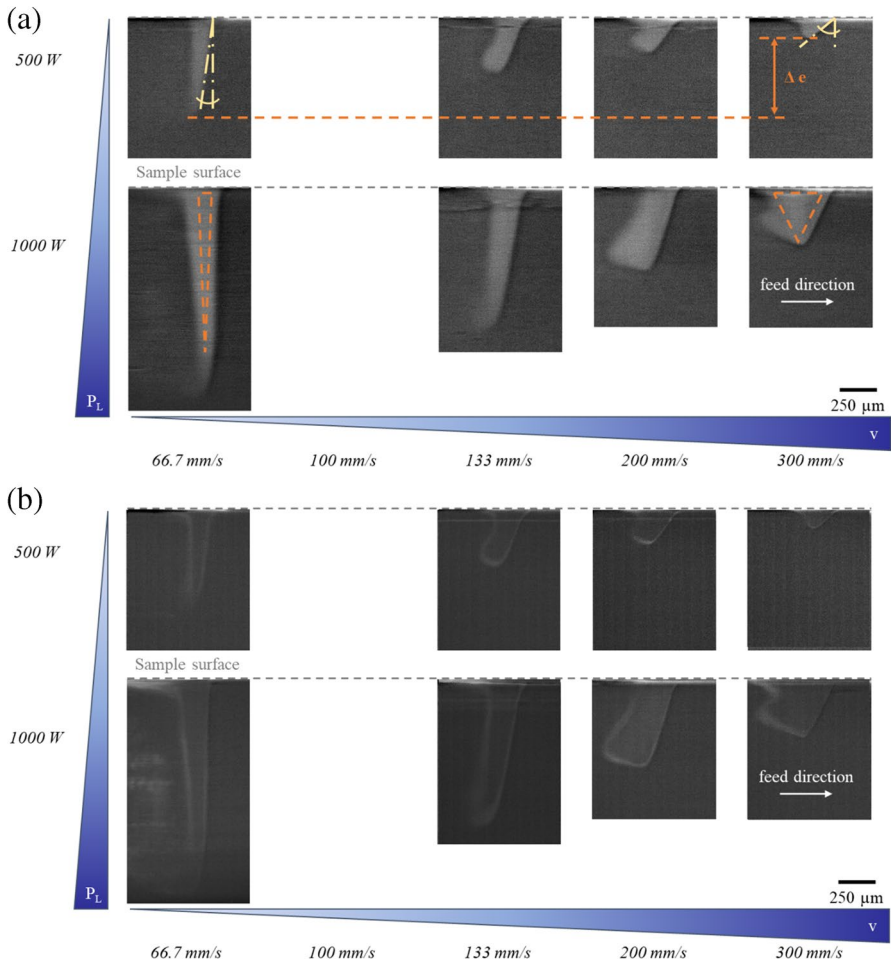


Fig. 6 Comparison of the vapor capillary geometry for laser beam welding of S235 JR, $t=2$ mm, $\lambda=1030$ nm, $d_p=200$ μm , $f=5000$ Hz; **a** temporal average and **b** standard deviation representation

part of the capillary in welding direction is found located near the keyhole tip for low feed rates. Increasing the welding speed changes the geometry into a U-shape (see schematic illustration in Fig. 7), as the bulge reaches the surface, causing a higher loss of reflected laser radiation. It is assumed that this finding is related to the increased number of multiple reflections caused by the lower absorptivity of copper for NIR radiation, as the absorptivity dependence of copper and steel on the angle of incidence is comparable at the melting temperature of the materials [8]. This aspect takes effect especially at high aspect ratios of the capillary respectively high line energies (low feed rate, increased laser power). The different areas and degrees of bulging can be identified by the added standard deviation images in Fig. 7, which, like for steel, particularly affect the rear wall. The widening of the capillary to the

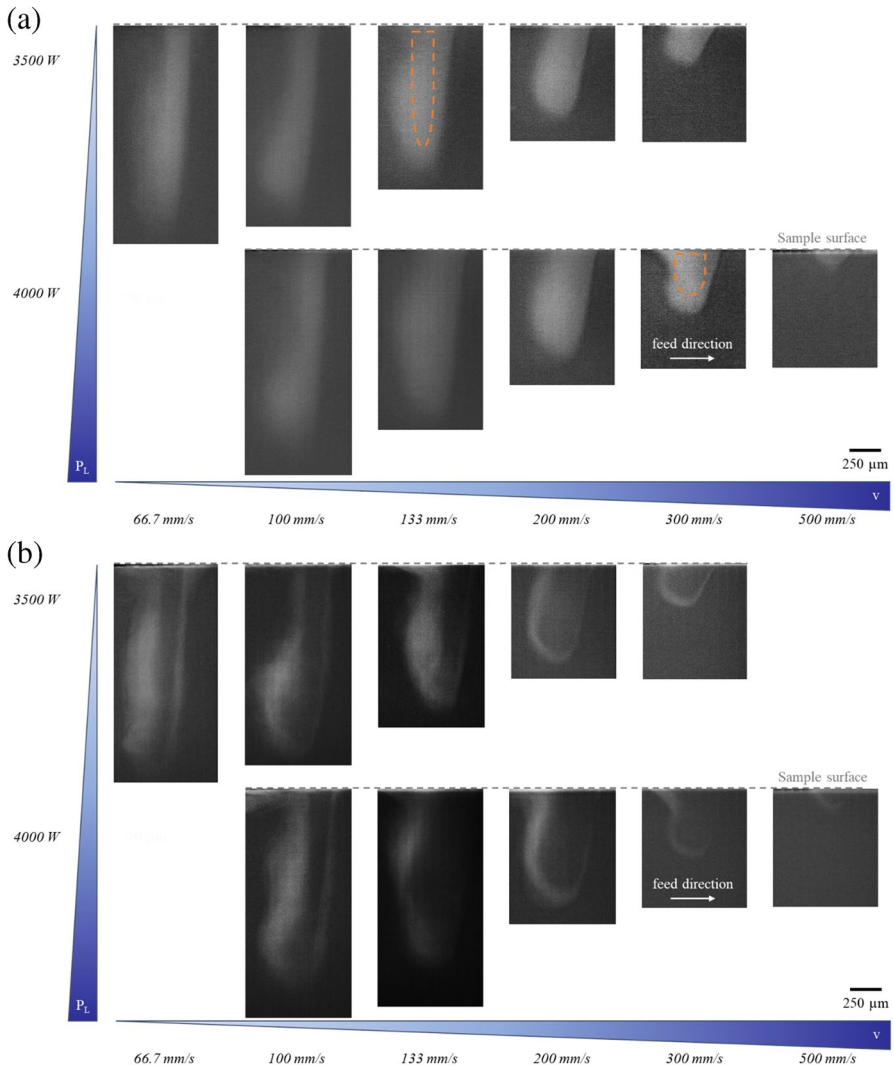


Fig. 7 Comparison of the vapor capillary geometry for laser beam welding of Cu-ETP, $t = 2$ mm, $\lambda = 1030$ nm, $d_p = 200$ μm , $f = 5000$ Hz; **a** temporal average and **b** standard deviation representation

upper sample surface is already noticeable from a feed rate of $v = 133$ mm/s, which is attributed to the lower surface tension of copper compared to steel, which acts as a closing pressure on the capillary [56]. At both laser powers presented, the penetration depth shows a stronger decrease, while the capillary front wall angle seems to be less sensitive to parameter changes compared to mild steel. This finding correlates with a shifted point of transition of the capillary into a V-shape, detectable for $v = 500$ mm/s at $P_L = 4$ kW, where the inclination of the front wall leads to a minor effect of the reflected laser power on the back wall.

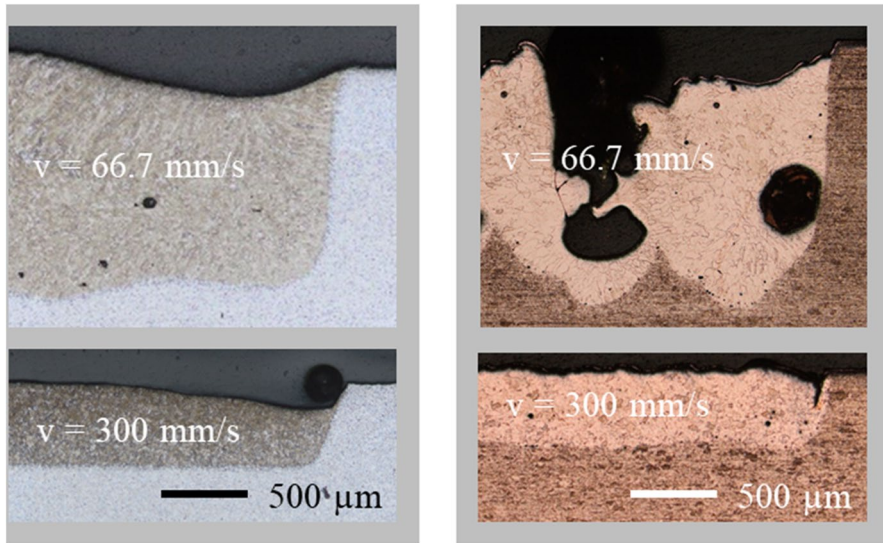


Fig. 8 Longitudinal sections of laser welds of S235 JR (left), $P_L = 1$ kW and Cu-ETP (right), $P_L = 3$ kW using $\lambda = 1030$ nm laser radiation

Table 5 Comparison of geometric circumstances in the laser matter interaction zone using in situ synchrotron X-ray imaging and metallographic preparation method for 1030 nm laser radiation

Dimension ($\Delta 66$ mm/s – 300 mm/s)	Unit	S235JR, $P = 1$ kW	Cu-ETP, $P = 3$ kW
Average depth decrease of the vapor capillary Δe	mm	1.05 (74%)	1.08 (78%)
Average penetration depth decrease Δe_{weld}	mm	0.97 (70%)	1.09 (77%)
Average capillary front wall angle increase $\Delta \alpha$	deg	22.3 (2108%)	20.5 (493%)
Average capillary front wall angle increase $\Delta \alpha_{\text{weld}}$	deg	21.8 (1211%)	19.2 (505%)

A comparison of the results with longitudinal sections from weld seams with selected parameter sets is shown in Fig. 8. The geometric conditions of the laser-matter interaction zone can be estimated by the analysis of an interrupted weld, i.e., when the laser is suddenly turned off and the keyhole front stays in a frozen state [57]. For this purpose, the weld seams were cut in their plane of symmetry in welding direction polished and prepared by electrochemical etching.

The quantitative comparison of the metallographic evaluation and of the determination of geometrical capillary features from in situ analysis using synchrotron X-ray imaging is given in Table 5. The X-ray results for Cu-ETP, $P = 3$ kW are taken from our previous investigation, presented in [26]. The relative ratios, calculated with reference to a feed rate increase from $v = 66.7$ mm/s to 300 mm/s, are listed in brackets. A good consistency of the in-situ analyses and metallographic findings is observed, especially for copper.

The higher degree of deviation for steel identifiable from the ratio comparison of the capillary front wall angle is assumed to be caused by the increased heat

accumulation according to the sample design in the in situ observations, as this leads to an excessive heat input at low feed rates in correlation with an underestimation of the capillary front wall angle (also compare Fig. 1). For copper welding, the high dynamics at low feed rates using NIR laser radiation can be observed from the highly fluctuating penetration depth in combination with an uneven, crater shaped sample surface at $P_L = 3 \text{ kW}$, $v = 66.7 \text{ mm/s}$.

Vapor Capillary Geometry of Steel and Copper Using 515 nm Processing Wavelength

Figures 9 and 10 show the evolution of the vapor capillary geometry for laser beam welding of steel and copper for laser power $P_L = 0.5 \text{ kW}$ and 1 kW and feed rate v from 66.7 mm/s to 300 mm/s using 515 nm laser radiation. For copper the laser power was set to 1.5 kW and 2 kW to produce weld seams in deep penetration mode.

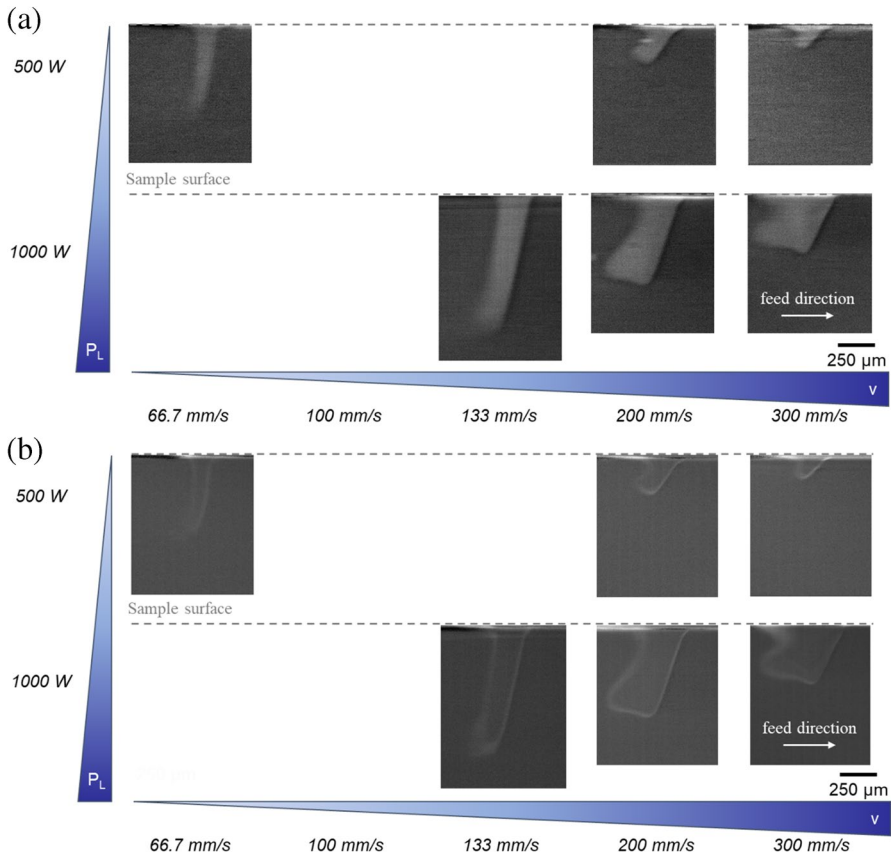


Fig. 9 Comparison of the vapor capillary geometry for laser beam welding of S235 JR, $t=2 \text{ mm}$, $\lambda=515 \text{ nm}$, $d_f=200 \mu\text{m}$, $f=5000 \text{ Hz}$; **a** temporal average and **b** standard deviation representation

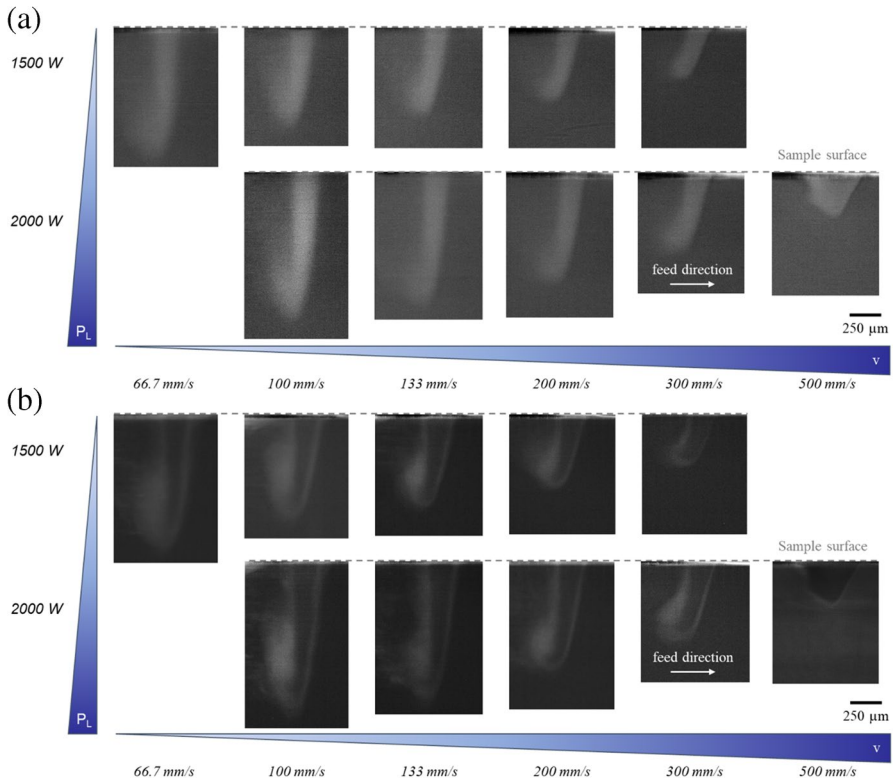


Fig. 10 Comparison of the vapor capillary geometry for laser beam welding of Cu-ETP, $t=2$ mm, $\lambda=515$ nm, $d_F=200$ μm , $f=5000$ Hz; **a** temporal average and **b** standard deviation representation

The qualitative comparison of Figs. 6 and 9 does not reveal significant differences in the geometry of the vapour capillary using 515 and 1030 nm laser radiation and their dynamic behaviour when analysing the standard deviation images. A similar behaviour in terms of the influence of the increase of laser power and feed rate variation with regard to the decrease of the capillary depth, the bulging of its back wall, as well as the increase of the front wall angle are observed. This finding can be attributed to the similar absorptivity of steel (approximated by optical data for iron, [58]) for both laser wavelengths, which is about 8% increased for 515 nm compared to 1030 nm radiation at melting temperature.

For copper, on the other hand, the use of green laser radiation considerably alters the vapour capillary geometry in the investigated parameter range of laser power and feed rate: The decrease in capillary depth is found significantly lower compared to the results for copper processing using NIR laser radiation presented in Fig. 7; a quantitative characterization will be given later in this work in combination with the discussion of the capillary front wall inclination. Compared to 1030 nm wavelength, the growth of the capillary aperture when the feed rate is increased (especially when the bulge reaches the sample surface) is not as

pronounced. Bright areas wider than the capillary entrance at the sample surface against the feed direction are recognizable at 66.7 mm/s and 100 mm/s in their lower half from standard deviation images, which can be attributed to the rapid geometry change when looking at the individual X-ray images. The mechanism of bulge formation is also observed in [26], although the increase in width is found less pronounced at 515 nm (also compare spatial expansion of vapor capillary geometry for feed rates $v \leq 100$ mm/s for 1030 nm and 515 nm laser radiation in Figs. 7 and 10). At higher feed rates $v > 100$ mm/s and both laser powers investigated, the bulge is concentrated to a limited area around the capillary tip, with the capillary geometry at the same time showing a smaller depth and an increased front wall angle.

In general, the fluctuating region is observed more concentrated in laser welding of copper using 515 nm laser radiation compared to the results for NIR laser radiation presented in “[Vapor Capillary Geometry of Steel and Copper Using 1030 nm Processing Wavelength](#)” section. This finding can be attributed to the increased absorptivity of copper for green laser radiation, which changes the energy distribution for a comparable aspect ratio of the capillary, as a higher amount of energy is deposited in the cavity wall with the first reflection. The decreasing white rim around the tip of the capillary (most distant point from the sample surface) is in good accordance with the lower depth variation of the final weld seam in longitudinal section shown in Fig. 11.

For steel, no significant differences can be observed from the comparison of the in situ observations and the metallographic results for 515 nm laser radiation and from the results for steel presented and discussed in “[Vapor Capillary Geometry of Steel and Copper Using 1030 nm Processing Wavelength](#)” section. In the case of

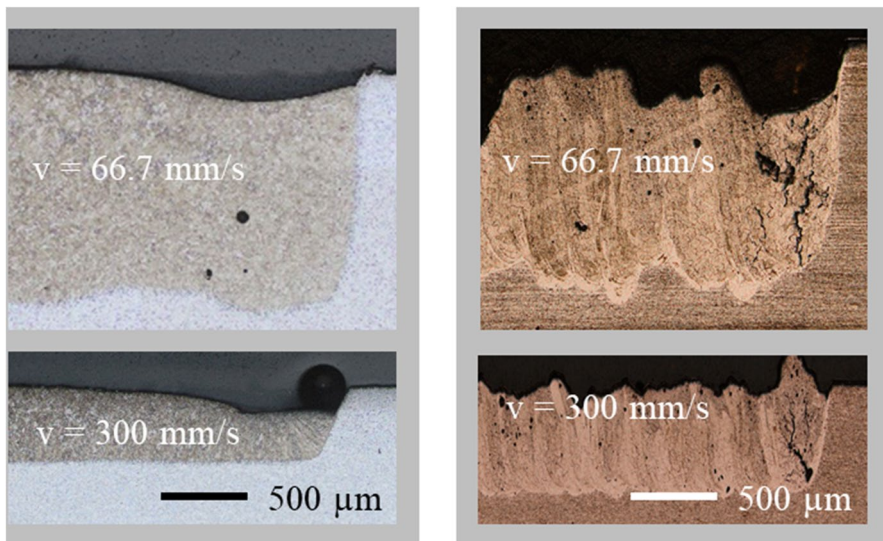


Fig. 11 Longitudinal sections of laser welds of S235 JR (left), $P_L = 1$ kW and Cu-ETP (right), $P_L = 2$ kW using $\lambda = 515$ nm laser radiation

copper, it can be observed that the capillary geometry converges to the capillary shape of steel due to the change in processing wavelength, while the diameter is of the same order of magnitude as the laser beam diameter. In addition, a less crater shaped sample surface of copper is found compared to NIR laser radiation for the low feed rate of $v=66.7$ mm/s, which is in good accordance with the investigations presented in [24]. Since the capillary bulge is observed in a more concentrated shape and also the dynamically fluctuating area around, the corresponding increase in vapour pressure is less pronounced and the ejection of larger parts from the melt pool is avoided.

The quantitative evaluation of the metallographic analysis together with the determination of the geometric capillary features from in situ analysis using synchrotron X-ray imaging is shown in Table 6. Again the relative ratios, calculated with reference to a feed rate increase from $v=66.7$ mm/s to 300 mm/s, are listed in brackets. Good agreement is found between the in-situ analyses and the metallographic findings, whereby again the discrepancy is greater for steel. As discussed in the previous section, the lower thermal conductivity of the material is assumed to be the reason for this result.

It can be noted from the capillary geometries that the transition point from an elongated cylindrical to a V-shape of the vapour capillary is observed at increased processing speed for copper compared to steel (observation at $v=300$ mm/s for steel, $v=500$ mm/s for copper welding). This observation is consistent for both materials at both laser wavelengths. This effect is related to the lower sensitivity of the inclination of the capillary front wall to the feed rate for copper compared to steel, recognisable from Tables 5 and 6. The turning point is characterized by an inclination angle at which the front wall is inclined to the point that the irradiated energy and the evaporation pressure induced thereby expand the capillary back wall against the capillary closing pressure (consisting of surface tension pressure, hydrostatic pressure and hydrodynamic pressure [28]) in feed direction. Since this state is a function of the beam diameter and the capillary front wall inclination angle [59], this situation arises at increased feed rate for copper compared to steel. This V-shape is reported to be correlated to the formation of humping and undercuts of the seam surface, for example when processing Aluminum described in [60]. This fact lead to an increased processing window for copper towards higher feed rates compared to steel for equal spot diameters, which is in good agreement with the results in [61], where the authors report on the calculation and measurement of the humping threshold for different materials.

Table 6 Comparison of geometric circumstances in the laser matter interaction zone using in situ synchrotron X-ray imaging and metallographic preparation method for 515 nm laser radiation

Dimension ($\Delta 66$ mm/s – 300 mm/s)	Unit	S235JR, P = 1 kW	Cu-ETP, P = 2 kW
Average depth decrease of the vapor capillary Δe	mm	1.07 (74%)	0.72 (53%)
Average penetration depth decrease Δe_{weld}	mm	0.99 (72%)	0.74 (54%)
Average capillary front wall angle increase $\Delta \alpha$	deg	24.1 (2407%)	11.3 (487%)
Average capillary front wall angle increase $\Delta \alpha_{\text{weld}}$	deg	20.4 (703%)	10.9 (507%)

Influence of Process Parameters on the Front Wall Inclination of the Vapor Capillary

The geometric conditions of the vapor capillaries described qualitatively in the two previous sections are plotted in Fig. 12 using mean values for all investigated parameter sets. In subgraphs (a) and c), the influence of the feed rate on the capillary front wall angle α is plotted for different laser powers and both laser wavelengths (515 nm/ 1030 nm) for steel at the top and copper at the bottom. The subgraphs (b) and d) on the right show the influence of the capillary depth (respectively aspect ratio of the capillary as a constant beam diameter is used in all investigations) on the capillary front wall angle for different laser powers and 515 nm as well as 1030 nm laser radiation for steel at the top and copper at the bottom respectively.

As already discussed in “Vapor Capillary Geometry of Steel and Copper Using 1030 nm Processing Wavelength” and “Vapor Capillary Geometry of Steel and Copper Using 515 nm Processing Wavelength” sections, the inclination angle of the front wall increases with an increase of the feed rate for both materials and both

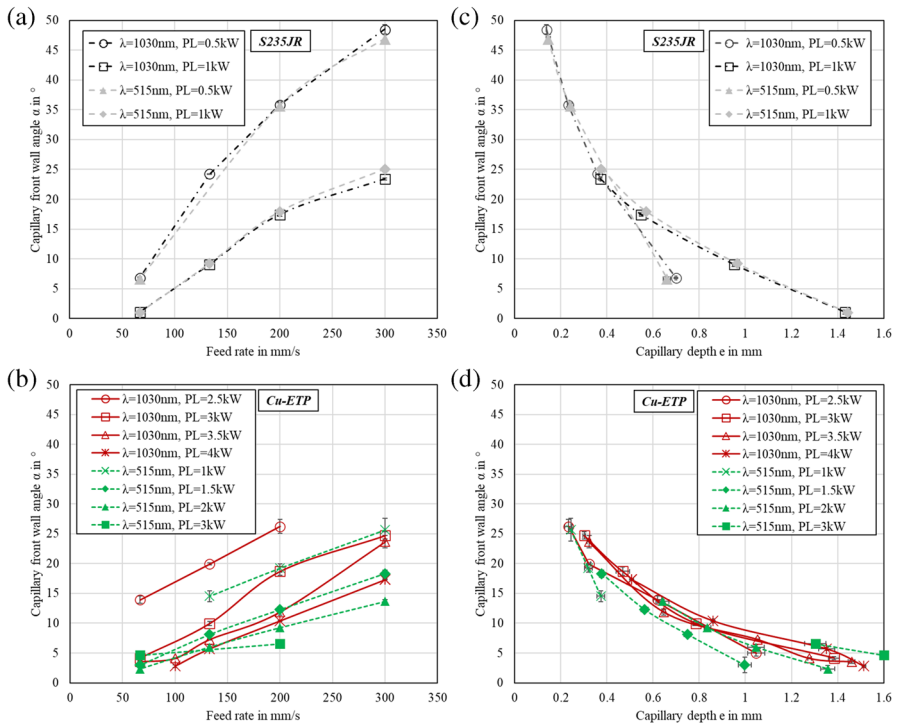


Fig. 12 Influence of process parameters on the front wall inclination of the vapor capillary: Left: Capillary front wall inclination versus feed rate for different laser powers and 515 and 1030 nm laser radiation; Right: Capillary front wall inclination versus capillary depth for different laser powers and 515 and 1030 nm laser radiation; Top: Results for mild steel S235JR (a) and c); Bottom: Results for Cu-ETP (b) and d))

wavelengths across all investigated laser powers. For steel, the values for $P_L = 0.5$ kW and $P_L = 1$ kW are well in line between the two wavelengths, which can be attributed to the similar absorptivity of the material in the investigated wavelength range of the laser beam sources. The data trend reveals lines through the origin that especially deviate at the feed rate of $v=66.7$ mm/s due to the underestimation of the inclination angle caused by the disproportionate heat accumulation in the interaction zone (see [Vapor Capillary Geometry of Steel and Copper Using 1030 nm Processing Wavelength](#) section). The slope of the data lines increases with increased laser power. Therefore, for the welds of S235JR (Fig. 12a), at the same feed rate of 133 mm/s, a capillary front wall angle of approx. 24° can be detected for a laser power of 0.5 kW whereas the value decreases to approx. 9° for $P_L = 1$ kW. As the feed rate increases, the capillary front angle increases, which is observed in comparable ratios for both laser wavelengths. These experimental findings suggest that by selecting the laser power, the front wall angle can be adjusted proportionally. However, the maximum angle per feed rate is limited by the deep penetration threshold of the material since the choice of a lower laser power will not initiate a deep penetration welding process.

The same behavior is evident for the Cu-ETP welds, nevertheless the data points for $\lambda=1030$ nm, $P_L = 2.5$ kW and $\lambda=515$ nm, $P_L = 1$ kW do not follow the determined trend. The welding process in these cases is not assumed to be developed as a total deep penetration welding process assuming a significant effect of multiple reflections, as the laser power was just above the material- and wavelength-dependent deep penetration threshold. Due to the stronger growth of the front angle with increasing feed rate for 1030 nm compared to 515 nm for equal laser power of $P_L = 3$ kW, a capillary front angle of $\alpha=6.5^\circ$ is achieved for 515 nm at a feed rate of $v=200$ mm/s whereas a capillary front angle of $\alpha=18.7^\circ$ is observed for 1030 nm at 200 mm/s. This difference is attributed to the increased effect of multiple reflections during copper welding using NIR laser radiation, since more energy is lost through reflections due to the opening of the aperture (see Fig. 7 compared to Fig. 10). In addition, less energy is deposited per beam interaction due to reduced absorptivity of NIR compared to green laser radiation.

The analysis in subplots b) and d) relates the inclination of the capillary front wall to the measured capillary depth, resp. aspect ratio. It can be seen that the values for both steel and copper show a quadratic decrease of the front wall inclination for an increased capillary depth. This trend can be observed for both laser wavelengths. By the selection of a higher laser power, an increase in the capillary depth can be generated for equal capillary front wall inclination angles, for example for copper the laser power increase from $P_L = 1.5$ kW to 2 kW at an inclination of approx. $\alpha=8^\circ$ is observed to increase the capillary depth for 515 nm laser radiation by $\Delta e=0.1$ mm. For 1030 nm wavelength, the increase from 3.5 kW to 4 kW at an inclination angle of approx. 10° leads to a measured depth increase of $\Delta e=0.05$ mm respectively. This stronger increase in capillary depth for $\Delta P=0.5$ kW for 515 nm is assumed to be related to the altered absorptivity for 515 nm compared to 1030 nm wavelength, leading to a more pronounced “drilling” of the capillary in beam propagation direction through the increased energy input. In addition, the aperture at the sample surface was observed narrower (see

Vapor Capillary Geometry of Steel and Copper Using 515 nm Processing Wavelength section), leading to less reflection losses compared to NIR laser radiation. This effect is also strengthened by the observation of a slightly deeper vapor capillary at the same front wall angle for NIR welding experiments over all data points on copper, which suggests that more energy is reflected into the capillary depth.

These results are in good agreement with the model developed in [59], where the author states that the maximum achievable penetration depth during welding is not achieved only by a single reflection of the incident laser radiation. Rather, the individual partial beams are directed into the capillary depth according to the principle of multiple reflection and result in an increase in capillary depth, which is drilled deeper with higher laser power. This fact also means that the number of internal capillary reflections decreases as the capillary depth decreases or a wider vapor capillary is present, equivalent to an increase in the capillary inclination angle with at constant feed rate. In the upper region of the capillary which is directly illuminated by the projected beam area, the characteristic beam parameters focal diameter and laser power in combination with the feed rate determine the capillary inclination angle α . Furthermore, the capillary depth increase due to the impact of multiple reflections results in the final capillary depth, whereby the inclination angle α tends to be increased, as the reflected beam is less energetic.

The results from Fig. 12b and d in combination with experimental findings for the capillary geometry of stainless steel reported in [62] are plotted in Fig. 13. In addition, the analytic description of the capillary inclination α from [59] in Eq. (2) is shown as an orange dashed line.

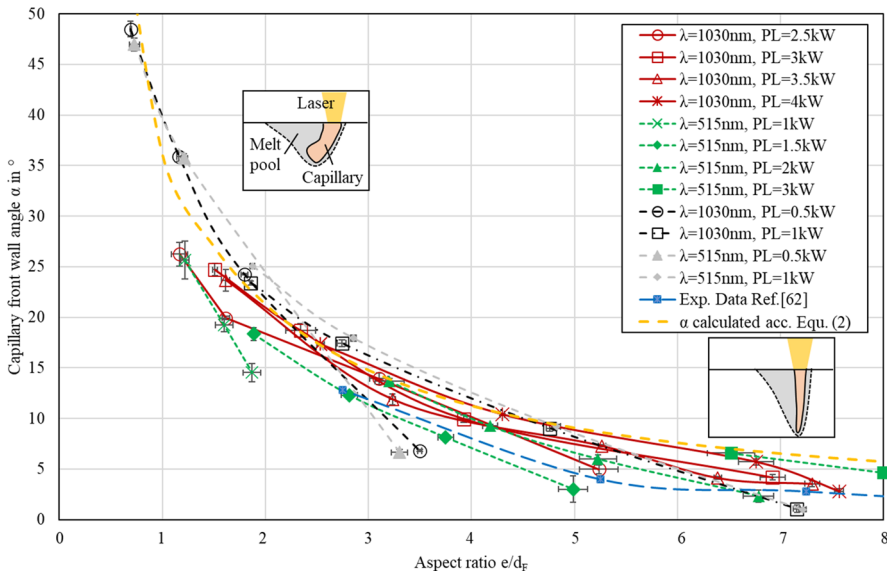


Fig. 13 Front wall inclination of the vapor capillary as a function of the aspect ratio of the vapor capillary (e/d_f) for varied laser power and feed rate using 515 and 1030 nm laser radiation for copper and steel

$$\alpha = c \cdot \arctan\left(\frac{1}{x}\right), \text{ with } x = \frac{e}{d_F} \quad (2)$$

where c is a correction factor which was assumed to be 0.8 for our investigations, e is the capillary depth, and d_F describing the focal diameter. Schematic illustrations of the capillary geometry for different aspect ratios are also shown.

The overlay of our investigations to the results of other researchers and theoretical descriptions in the interaction zone shows a good agreement. Figure 13 emphasizes that the capillary inclination angle decreases with increasing aspect ratio (e/d_F) of the weld seam. A closer look at the values also reveals that an increase of the line energy results in smaller inclination angles of the capillary geometry. For example, the data points $P_L = 4$ kW and $v = 133.3$ mm/s (red x) and $P_L = 3$ kW and $v = 66.7$ mm/s (red cuboid) for $\lambda = 1030$ nm when processing copper for an aspect ratio of approx. 7, resulting in line energies of $E_L = 30$ J/mm and $E_L = 45$ J/mm respectively, are observed with a $\Delta\alpha = 1.5^\circ$ smaller inclination angle of the capillary front wall for the higher E_L . This effect is observed to be stronger for copper at 515 nm wavelength looking at the spatial separation of the trend lines, as the absorptivity for copper in the NIR wavelength range is significantly lower compared to green laser radiation.

According to the findings of Weberpals [59], due to a self-regulating mechanism between the capillary front wall inclination and the irradiated intensity, the absorbed intensity on the front wall is only dependent on the feed rate v . Consequently, if the feed rate is constant, the inclination of the capillary front wall decreases due to an increase of the irradiated intensity, equivalent to an increase of the line energy at constant spot diameter as in this work. This correlation is shown in Eq. (3), where I_0 denotes the irradiated intensity.

$$\alpha \sim \frac{v}{I_0} \sim \frac{v \cdot d_F^2}{P_L} \quad (3)$$

When looking at the results for steel welding, the data points are observed following the same behavior, however significantly lower line energies for the same spot diameter are needed compared to copper (as the feed rate range is identical in the presented investigations, see significantly lower laser power used). This fact is assumed to result from the different thermal conductivity of both materials (see. Table 1), promoting the energy input in the interaction zone and lowering the heat flow into the surrounding base material for steel compared to copper. In addition, by the inclusion of the results presented in [62] it can be seen that with increasing beam diameter d_F ($d_F = 400$ μm in Ref. [62]) and thus decreasing focusability, the respective data points move downwards. A similar front wall inclination angle is thus obtained at smaller aspect ratios of the capillary, indicating that capillary internal reflections decrease as a result of the lower focusability.

It is therefore assumed that the use of a smaller beam diameter has an increased effect on the process zone shape for copper using 1030 nm laser radiation compared to 515 nm laser radiation, since multiple reflections are observed to be increased for the former (see capillary geometries for laser welding of copper using 1030 nm laser

radiation, which show a pronounced widening in feed direction in temporal average images from in-situ observations, Fig. 7).

Analysis of Energy Coupling in the Capillary Front Wall

In order to quantify the interaction of the vapor capillary geometry with the laser radiation, a pixel-wise measurement of the capillary front wall profiles was carried out using image processing of the temporal average images by binarization and median filtering. The results are shown as an example for Cu-ETP using 1030 nm processing wavelength at a laser power $P_L = 3500$ W in Fig. 14. Based on these curves, the local angles of incidence of the laser radiation on the vapor capillary front wall were calculated as a function of the capillary depth e , assuming a smooth capillary surface and a beam incident perpendicularly on the capillary, see Fig. 14 on the right.

Since the capillary front wall at $P_L = 3500$ W and $v = 66$ mm/s is almost vertical in the middle capillary region, angles of incidence close to 90° are observed for this parameter set. It is also noteworthy that the local angles of incidence for feed rates between 66 mm/s and 133 mm/s at vapor capillary depths between 2.1 mm and 1.5 mm are found in a similar range of values between 70° and 90° .

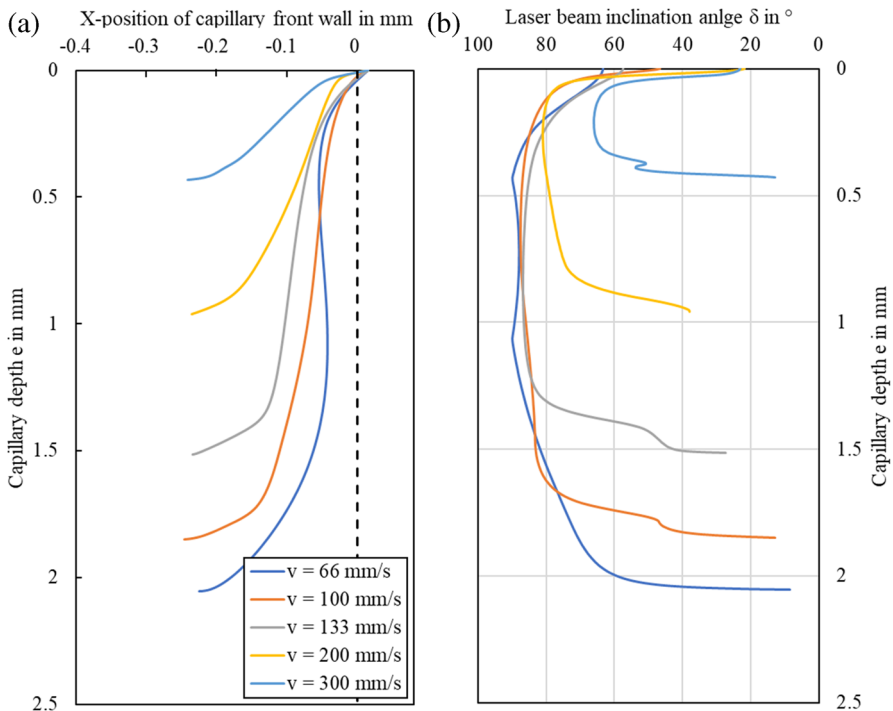


Fig. 14 Capillary front wall profiles (a) and local angles of incidence calculated from these (b) as a function of feed rate and capillary depth e for Cu-ETP, $P_L = 3500$ W, $\lambda = 1030$ nm

If the feed rate is increased further, the local angles of incidence decrease, reaching values at around 50° at $v = 300$ mm/s and $P_L = 3500$ W. For all feed rates investigated, the angles of incidence decrease sharply from about $\frac{3}{4}$ of the maximum capillary depth, as the capillary bottom forms there.

The angular dependence of the absorptivity of copper and iron is shown in Fig. 15, calculated from the reflectivity [2] with measured data for the refractive index n and the absorption index k from [22] for copper and [58] for iron. In the graphs (a) and (b) a difference between room temperature and an elevated temperature close to the melting temperature can be identified for both materials. For copper, the wavelength dependent difference between 0.5 and 1 μm decreases with increasing temperature, while the brewster maximum becomes slightly more prominent. For iron, on the other hand, a slightly higher difference between the wavelengths can be observed in combination with a strong reduction of the angular dependence (Best identifiable near the brewster maximum between 70° and 80°). For the evaporation during deep penetration welding, the absorbed intensity distributed on the irradiated surface is decisive, which can be described according to Eq. (4) as

$$I_A = I_0 \cdot A(\delta, \lambda) \cdot \cos(\delta) \quad (4)$$

where I_0 denotes the irradiated intensity, A the angle and wavelength-dependent absorptivity and δ the angle of incidence. As only the projection $\cos(\delta)$ of the surface perpendicular to the direction of incidence serves as the effective receiving surface in the case of irradiation under an angle, a multiplication by the cosine factor is introduced.

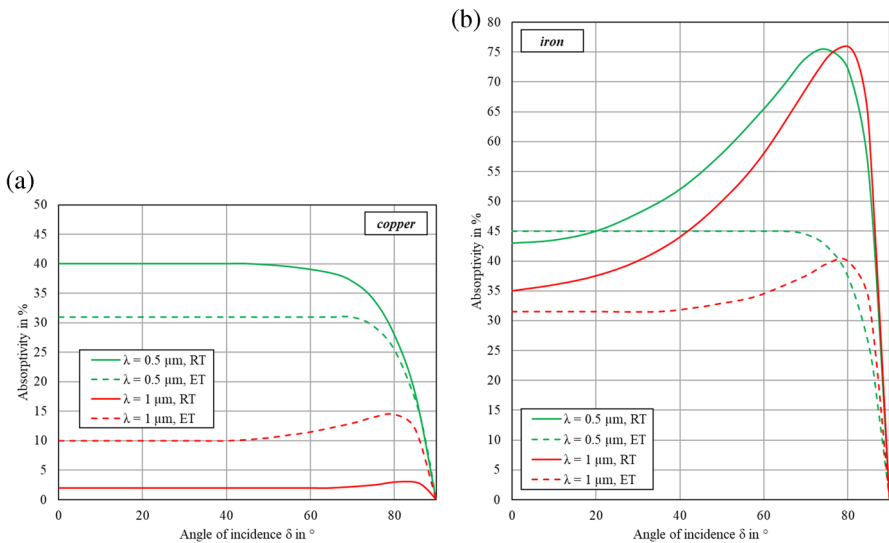


Fig. 15 Angular dependence of the absorptivity of copper (a) and iron (b) at 0.5 and 1.0 μm at room temperature (RT) and elevated temperature (ET, copper = 1400 K; ET, iron = 1800 K).

Based in Fig. 15 and Eq. (4), the ratio I_A/I_0 in % is plotted for the capillary front wall profiles to illustrate the energy coupling for the first laser interaction for both materials and both laser wavelengths in Fig. 16. Due to decreasing angles of incidence with increasing feed rate, the average ratio I_A/I_0 for Cu-ETP increases for 515 and 1030 nm laser radiation, meaning that a higher portion of the irradiated energy is introduced into the front wall. This trend can also be observed for steel in the visible wavelength range (515 nm). In contrast, a slightly negative trend is present for S235JR with NIR laser radiation, caused by the presented behavior of the optical properties. In quantitative terms, the ratio I_A/I_0 at 515 nm and copper is well above 10% for $v \geq 100$ mm/s, while at 1030 nm it is observed to be $\leq 15\%$ for all parameters investigated. Therefore, less energy is deposited per beam interaction due to the reduced absorptivity of NIR compared to green laser radiation (also see Fig. 15). For the mild steel, I_A/I_0 -values in the range of 30–40% are identified from a velocity $v > 100$ mm/s at 1030 nm, and at 515 nm slightly above that. Over the materials and wavelengths, the I_A/I_0 values drop to

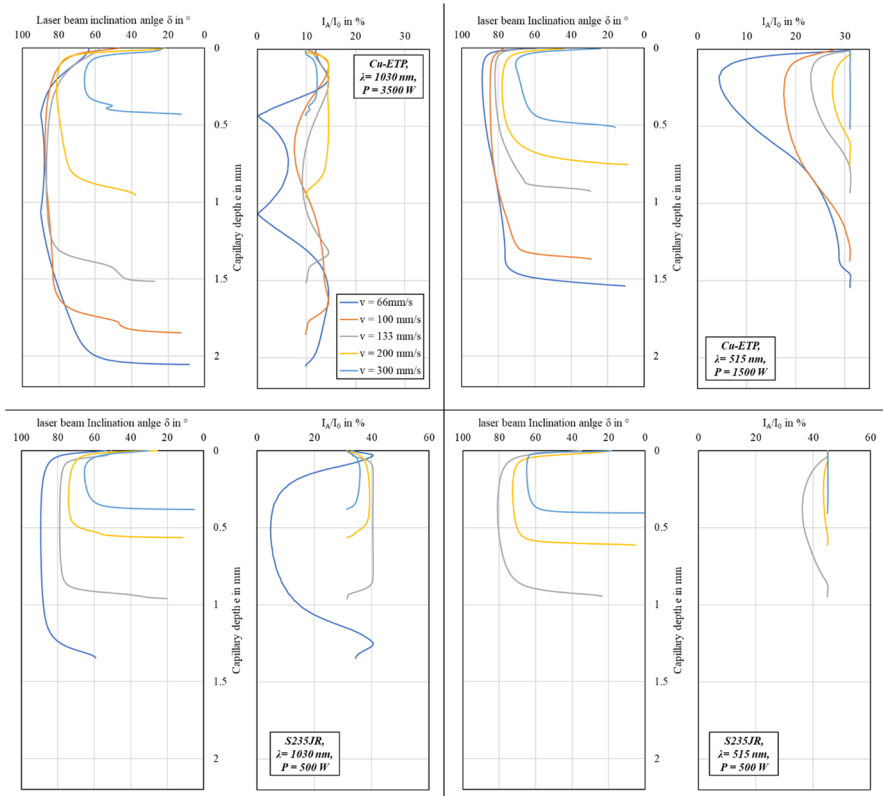


Fig. 16 Local angles of incidence calculated from capillary front wall profiles (each left) and I_A/I_0 as a function of capillary depth e and feed rate v (color coding applies to all subgraphs) for Cu-ETP (top) and S235 JR (bottom), further process parameters see inserts

single-digit values at low feed rates due to the small local inclination angles, as evident from the dark blue curves in Fig. 16. Consequently, the direct irradiation of the capillary front wall plays a subordinate role for energy coupling in this situation, and multiple reflections are significantly involved.

In Fig. 17, the calculated ratio in % is plotted for the mean values of the local angles of incidence (see Fig. 16), with the capillary bottom excluded from the calculation. Again, the values for the optical material constants shown in Fig. 15 are used. The dashed lines depict linear fits of the data points per material and wavelength. It becomes apparent that the trend curves describe the feed rate dependency of the I_A/I_0 ratio very well.

The calculated ratio between absorbed intensity and irradiated intensity increases approximately linearly with increasing feed rate from 0.7% at $v=66$ mm/s to 5.7% at $v=300$ mm/s for Cu-ETP using $P_L = 3500$ W 1030 nm laser radiation. Assuming that the intensity distribution is constant for all feed rates, an increased feed rate is thus accompanied by an increase in the absorbed intensity at the capillary front wall. This ratio roughly triples when 515 nm instead of 1030 nm laser radiation is used for copper (Cu-ETP), which reinforces the statements and explanations of the observations presented in the previous sections.

In a comparison of the materials, the proportion of energy that is coupled into the capillary front wall of mild steel during the first interaction is significantly increased for NIR and green laser radiation compared to copper and ranges between 10% and 23% for $v > 100$ mm/s. Only the underestimation of the front wall inclination caused by the disproportionate heat accumulation in the interaction zone (see [Vapor Capillary Geometry of Steel and Copper Using 1030 nm Processing Wavelength](#) section) shifts the data trend for S235JR and 1030 nm laser radiation to lower I_A/I_0 values for $v < 100$ mm/s.

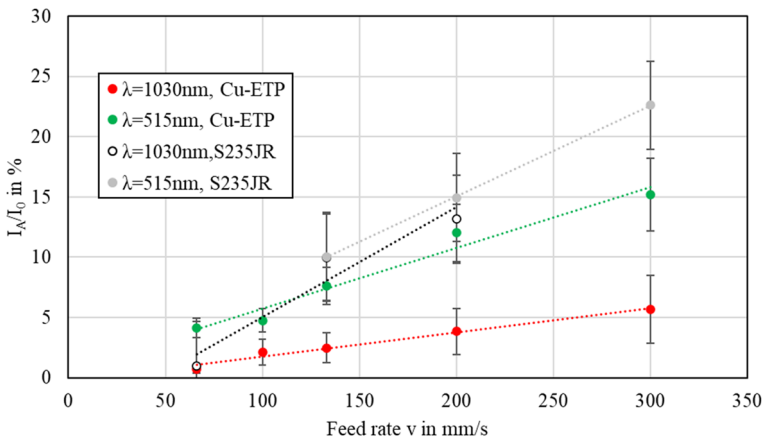


Fig. 17 I_A/I_0 calculated according to Eq. (4) for mean values of the local angles of incidence versus feed rate for Cu-ETP and S235JR using 515 and 1030 nm laser radiation

Analysis of Vapor Capillary Bulging

So far, the front wall inclination of the capillary and their local curvature have been widely considered during this work. The melt flow and the resulting surface quality of the weld seam are also strongly influenced by the vapor capillary geometry. To study the observed bulging and its relation to the surface quality of the weld bead in more detail, geometrical analyses based on the temporal average images and the final weld seams were carried out. Different parameters were evaluated, i.e. time-averaged characteristics were obtained for the capillary aperture at the sample surface d , the capillary depth e , the maximum of the capillary bulging a and the depth of the maximum bulging e_B (see insert in Fig. 18). The value maximum bulging a represents the maximum width of the vapor capillary in feed direction, meaning that the inclination of its front wall is also taken into account. Using the ratio formation, the maximum bulging a is related to the capillary aperture d and its depth e_B to the capillary depth e . The ratio e_B / e for copper and mild steel using 515 and 1030 nm laser radiation is plotted versus a / d in Fig. 18.

The larger dot per data series represents the mean value, together with the standard deviation of the depth of the maximum bulging (e_B / e) and the ratio a / d calculated from the individual data points. For the capillaries investigated in mild steel, a limited bulging with a / d ratios around 1 at 80% of the capillary depth is observed, not indicating significant differences for NIR and green laser radiation. For Cu-ETP, the mean value for 515 nm wavelength is close to these values with $e_B / e = 0.77$ and increased $a / d = 1.2$, while a promoted bulging ($a / d = 1.47$ at an average of 64% of the capillary depth) is found for 1030 nm laser radiation. This behavior is correlated with the increased number of multiple reflections for NIR laser radiation and copper, as analyzed in the previous sections.

The evaluation of the seam surface roughness for the welded copper samples by scanning with a 3D-profilometer (Keyence VR-6000, Keyence GmbH,

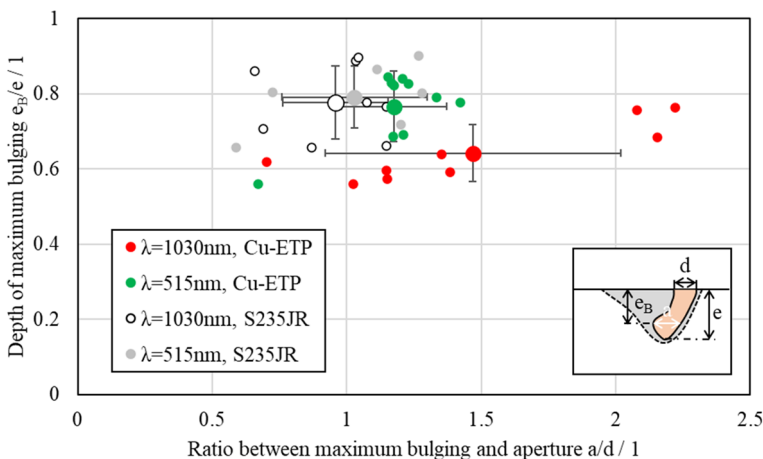


Fig. 18 Position of maximum bulging and related enlargement of the keyhole in feed rate direction

Neu-Isenburg, Germany) and averaging five line profiles in the weld direction, summarized to a mean value of the surface roughness R_a , is shown in Fig. 19. The values are plotted versus the measured aspect ratio of the weld seam on the x-axis with the penetration depth divided by the weld seam width. Since the seam width is measured wider for 1030 nm and Cu-ETP in the investigated parameter range (also see investigations in [8]), the metallographic aspect ratios are smaller for 1030 nm laser radiation.

For both laser wavelengths, trends towards higher average surface roughness of the weld seam R_a for increased aspect ratios are observable. Reasons for this behavior are higher dynamics in the interaction zone due to the increased evaporation pressure (Influence of Process Parameters on the Front Wall Inclination of the Vapor Capillary section).

A combination of the evaluations from Figs. 18 and 19 reveals that the observed bulging behavior can be associated with increased R_a values of the weld seam surface for copper using 1030 nm laser radiation. Consequently, the capillary bulging is related to the surface quality through its effect on the flow characteristics in the melt pool, which are discussed in the following section.

Analysis of the Characteristic Melt Flow During Laser Beam Welding

To better understand besides the influence of the process parameters also the changes in the characteristics of the dynamic effects in the melt pool caused by the recoil pressure of evaporation in the capillary and the melt flow around, the method described in “Data Evaluation – Image Processing and Analysis of the Velocity Field of the Melt Pool” section was applied to selected X-ray videos in order to calculate the characteristic melt pool for laser welding of copper and steel using the same spot diameter of $d_F = 200 \mu\text{m}$. For the purpose of comparison of the process zone for both materials, a similar capillary depth at a feed rate of $v = 133 \text{ mm/s}$ was selected for 1030 nm laser radiation. Temporal average images and the standard

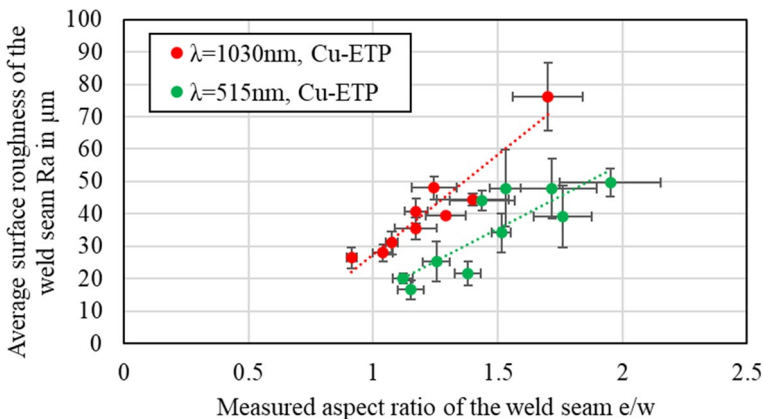


Fig. 19 Average surface roughness and measured aspect ratio of the weld seam for laser beam welding of copper, $d_F = 200 \mu\text{m}$

deviation representation in a square region of interest around the vapor capillary are shown in Fig. 20. It can be clearly seen that the capillary when welding copper using NIR laser radiation is much wider in feed direction compared to steel and a strongly fluctuating area is present near their rear wall. In addition, the melt pool is found increased for copper, which indicates, that more energy is absorbed in the irradiated area. By contrast, the calculation of the melt efficiency according to [63] for both parameter sets (copper: $P_L = 3.5$ kW, steel: $P_L = 1$ kW, material properties see Table 1) reveals a 60% increased value for steel compared to the copper welding process. The melt pool depth below the capillary decreases approximately linearly towards the sample surface for both metals. The analysis of single images from the X-ray videos shows that not just the capillary geometry alters over time caused by varying energy input on their front wall [64], but also the shape of the melt pool and its depth follow the dynamic changes of the latter. The observation of the parameter variation reveals that the change in the capillary geometry over the feed rate is also correlated with a change in the shape of the melt pool. For increasing feed rate the melt pool elongates and its shape alters from a quarter circle to a wedge like shape that follow the geometry of the vapor capillary. This behavior was also observed by the authors in [65] during laser beam welding of high-alloyed aluminum specimen.

The comparison of characteristic melt flows in the laser-matter interaction zone is shown in Fig. 21. For this evaluation, the shape of the melt pool was extracted from the average images, which give an average representation of the quasi-stationary welding process over time. Additionally, the vapor capillary geometries are shown in grey.

The velocity field is very inhomogeneous and dominated by eddies for steel as well as for copper. At the upper part of the capillary, the melt is observed to be driven partly downwards (clockwise rotating eddy) for steel, while at the lower

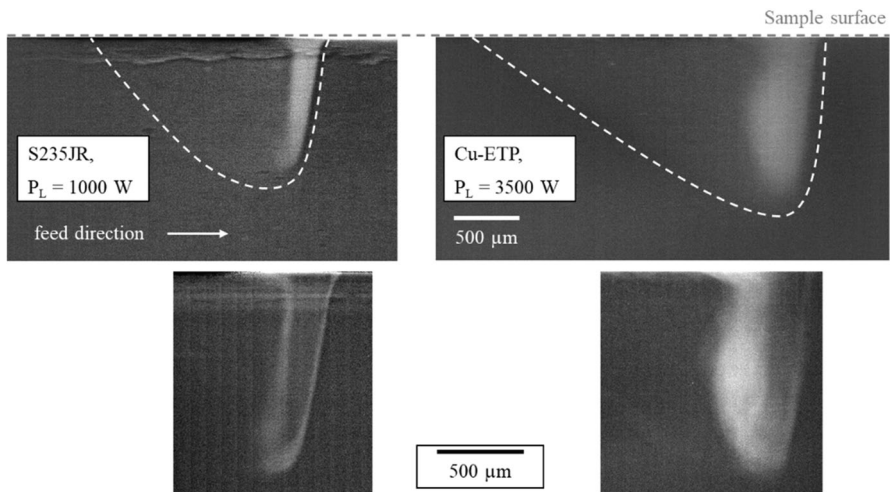


Fig. 20 Comparison of the vapor capillary geometry and melt pool dimensions for laser beam welding of mild steel and copper, $t = 2$ mm, $\lambda = 1030$ nm, $d_F = 200$ μ m, $f = 5000$ Hz

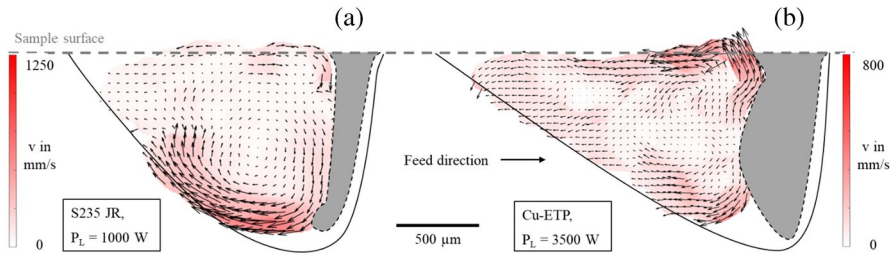


Fig. 21 Distribution of the averaged melt flow velocity for **a** S235JR, $P_L = 1$ kW and **b** Cu-ETP, $P_L = 3.5$ kW at a feed rate of $v = 133.3$ mm/s, $t = 2$ mm, $\lambda = 1030$ nm, $d_F = 200$ μ m, $f = 5000$ Hz. The color and length of the arrows represents the local melt flow velocity, the direction of the arrow indicates the flow direction. The black contour shows the mean melt pool shape also extracted from the X-ray images; the grey area shows the vapor capillary geometry

part the melt is driven towards the tip of the capillary. These flow patterns arise from an interaction of the capillary flow, the metal vapor induced flow as well as effects of the surface tension of the processed material [3], resulting in different flow directions and melt velocities depending on the melt pool region. For copper, the lower eddy in the region of the capillary tip is observed to be less pronounced, while the melt pool region close to the sample surface indicates a strong material movement from the deeper melt pool area towards the back rim end of the capillary and above. The observations for steel are in good accordance with investigations in [45] and experimental results from [66].

With regard to the maximum flow velocities, significantly higher values are found for steel compared to copper when considering the equal capillary depth. The maximum velocities are generally observed close to the bulging areas of the capillaries, thus in the case of steel at the capillary tip close to the deepest point of the melt pool, where the formation of process pores has been observed by other researchers, for example in [67]. For copper, the regions are close to the melt pool top surface located at the upper end of the bulging area and secondly near the capillary tip. The quantitative values confirm theoretical considerations and simulations in [28], which state that the maximum velocity of the melt can exceed 1 m/s and is thus significantly higher than the feed rate used. In addition, it is concluded that the flow around the capillary dominates in this feed rate range for steel, while the influence of this flow is less pronounced for copper and becomes predominant only at higher feed rates [28]. The influence of the melt flow around the capillary increases with decreasing thermal diffusivity and especially with decreasing difference between evaporation and melting temperature, which is experimentally observed in higher melt flow velocities for steel compared to copper. Therefore, the melt flow in this feed rate range for copper is more strongly determined by the metal vapour emerging from the capillary, inducing shear stresses on its wall, and the temperature dependence of the surface tension. All of these mechanisms lead to recirculating melt flows, mixing the liquid metal in the melt pool, changing the temperature distribution, and influence the weld seam geometry.

Moreover, the part of the kinetic energy transported through the melt flow to the end of the melt pool can be observed, which leads to melt pool swellings on the sample surface (also see Fig. 4). This swelling is particularly pronounced in copper welding using 1030 nm laser radiation near the back wall of the vapour capillary. This dynamic area can be correlated with the initiation region of spatter formation investigated in [19] Comparing the mass loss from defect generation during the welding process, which was determined by weighting the samples prior and after welding and relating this value to the molten volume from cross-sectional analysis, a percentage of 0.4% is obtained for steel, while a value of 1.5% is observed for the copper parameter set. It is therefore assumed that the identified difference in melt deflection at the surface for copper compared to steel initiates the pronounced defect formation.

Accordingly the vapor shear stress increases when 515 nm laser radiation is applied in copper welding, as the capillary geometry is found to be narrower in welding direction. Since for the green laser setup the weld length is limited (for kW-laser power) due to the pulsed operation mode the system was used in, data points for the analysis of the average melting velocities are currently not available for the evaluation. However, this statement can be correlated with the observation of a steady and also at higher feed rates increased formation of melt ejections for copper for 515 nm compared to 1030 nm laser radiation reported in Ref. [24].

Conclusion

The aim of this study was to reveal the changes and challenges in copper welding compared to well studied laser beam welding of steel, also looking at the capabilities provided by the use of visible laser radiation available in kW-class nowadays. In-situ synchrotron X-ray imaging was used to obtain a 2D view of the laser-matter interaction zone for Cu-ETP and S235JR with high temporal and spatial resolution using 515 and 1030 nm laser radiation with equal beam diameter. The generated X-ray videos were qualitatively and quantitatively evaluated using statistical measures and complex methods providing an insight on dynamic and averaged process conditions not accessible with conventional process observation techniques. Thus the effect of the different material properties and the influence of process parameters on the dynamic behavior of the vapor capillary and melt pool geometry in laser beam welding could be studied. Considering that the capillary front wall and its inclination is a complex physical phenomenon influenced by the irradiated laser power, which is mostly absorbed there, and the fluid flow around, and that its characteristics are of essential relevance for the formation of the laser welding process, its parameter dependency was investigated in detail. By comparing the experimental results with existing model representations and incorporating the results obtained from other researchers, the basic understanding of the phenomena dominating the interaction between irradiated laser radiation and the welded metal could be expanded.

The following conclusions can be drawn:

- The capillary geometries of copper generally show an increased dynamic behavior compared to mild steel, evident from the bulging of their back wall when examining the standard deviation of the X-ray videos. These dynamics are observed to be more pronounced for 1030 nm compared to 515 nm laser radiation due to an increased amount of capillary internal multiple reflections.
- The increase of the feed rate leads to an inclination of the vapor capillary front wall against feed direction and the increase of the laser power at constant feed rate causes a decrease of the inclination angle due to the increasing forces induced by the recoil pressure of evaporation.
- Considering I_A/I_0 at the front wall of the capillary during the first interaction, an increased feed rate is accompanied by an increase in the absorbed intensity there. No significant differences are identified for mild steel, while the calculation based on optical properties of the materials reveals a tripled ratio for 515 nm compared to 1030 nm laser radiation.
- A different sensitivity of the capillary geometry versus parameter variation is found for mild steel compared to copper, with the transition point of the capillary from an elongated cylindrical shape to a V-shape detected at higher feed rates for copper. The comparison with model representations and correlations derived therefrom shows that the capillary inclination angle decreases quadratically with increasing aspect ratio (e/d_F) of the vapor capillary, which applies consistently for both materials investigated.
- By the selection of a higher laser power, an increase in the capillary depth can be generated for equal capillary front wall inclination angles.
- A combined evaluation of the geometric features of the capillary bulging and the surface roughness of the final weld seams reveals a wavelength-dependent correlation for copper. The promoted bulging using 1030 nm laser radiation, on average closer to the sample top surface, is associated with increased Ra values (rougher weld seam).
- The analysis of the characteristic melt flow from tracer particle trajectories reveals that the velocity field is very inhomogeneous and dominated by eddies for steel as well as copper. Differences in terms of maximum average melt velocities and the area of their occurrence are detected. The different material-specific physical properties, especially thermal conductivity and surface tension, lead to varying melt pool dynamics and a pronounced eddy close to the melt pool surface for copper using 1030 nm laser radiation, which is assumed to be causal for the observation of pronounced spatter formation during copper welding in a certain process window.

In sum, the laser beam welding process of copper shows significantly increased dynamics in the interaction zone, both in the vapor capillary and through the observed strong melt acceleration near the sample surface. As shown, a change in energy input and its distribution over the capillary depth can be addressed through the use of 515 nm laser radiation, nevertheless, the calming of the dynamics is a major challenge for future work. Thereby, a combination of energy-efficiency and precise process guidance with regard to weld seam depth and defect prevention should result.

Acknowledgements This research was supported by TRUMPF GmbH & Co. KG and IPG Laser GmbH. The presented investigations were carried out in cooperation with RWTH Aachen University within the framework of the Collaborative Research Centre SFB1120-236616214 “Bauteilpräzision durch Beherrschung von Schmelze und Erstarrung in Produktionsprozessen” and funded by the Deutsche Forschungsgemeinschaft e.V. (DFG, German Research Foundation). The presented investigations were carried out in cooperation with DESY in Hamburg at PETRA III, and we would like to thank F. Beckmann and J. Moosmann for assistance in using P07 EH4. Beamtime was allocated for proposal I-20210713. The sponsorship and support are gratefully acknowledged. We would like to thank all people involved for their support.

Author Contributions Conceptualization, F.K.; methodology, F.K.; validation, F.K.; formal analysis, F.K.; investigation, F.K., J.S., M.H., C.S., F.B. and J.M.; resources, M.S.; data curation, F.K.; writing—original draft preparation, F.K.; writing—review and editing, F.K., S.R.; visualization, F.K.; supervision, S.R. and M.S.; project administration, M.S. and A.O.; funding acquisition, M.S.

Funding Open Access funding enabled and organized by Projekt DEAL. The authors gratefully thank the German Ministry for Economic affairs and Climate action for funding part of this work in the research project “GreenPIs: Laserbearbeitungseinheit für hochreflektive Werkstoffe” (Grant No KK5004303LP0) as part of the Central Innovation Pro-gramme for SMEs. The presented investigations were carried out within the framework of Re-search Unit FOR-5134, “Solidification Cracks during Laser Beam Welding: High Performance Computing for High Performance Processing,” (Grant No 434946896) and funded by the Deutsche Forschungsgemeinschaft e.V. (DFG, German Research Foundation). The sponsorship and support are gratefully acknowledged.

Data Availability The data sets generated during and analyzed during the current study are available from the corresponding author on reasonable request.

Declarations

Ethics Approval The authors respect the ethical guidelines of the journal.

Consent to Participate Not applicable.

Consent for Publication Not applicable.

Competing Interests The authors declare no competing interests.

Conflict of Interest The authors declare no conflict of interest. The funders had no role in the design of the study; in the collection, analyses, or interpretation of data; in the writing of the manuscript; or in the decision to publish the results.

Open Access This article is licensed under a Creative Commons Attribution 4.0 International License, which permits use, sharing, adaptation, distribution and reproduction in any medium or format, as long as you give appropriate credit to the original author(s) and the source, provide a link to the Creative Commons licence, and indicate if changes were made. The images or other third party material in this article are included in the article’s Creative Commons licence, unless indicated otherwise in a credit line to the material. If material is not included in the article’s Creative Commons licence and your intended use is not permitted by statutory regulation or exceeds the permitted use, you will need to obtain permission directly from the copyright holder. To view a copy of this licence, visit <http://creativecommons.org/licenses/by/4.0/>.

References

1. Communication from the Commission to the European Parliament, the Council, the European Economic and Social Committee and the Committee of the Regions: 'Fit for 55': delivering the EU's 2030 Climate Target on the way to climate neutrality. European Commission, Brussels (2021)
2. Michaelis, S., Schüttrumpf, J., et al.: VDMA - Roadmap Battery Production Equipment. 2030. VDMA Battery Production, Frankfurt am Main (2023)
3. Hügel, H., Graf, T.: *Materialbearbeitung mit Laser. Grundlagen und Verfahren*, 4th edn. Springer eBook Collection. Springer Vieweg, Wiesbaden (2022)
4. Abhishek Das, Li, D., Williams, D., Greenwood, D.: *Joining Technologies for Automotive Battery Systems Manufacturing*. <https://www.mdpi.com/2032-6653/9/2/22> (2018). Accessed 6 June 2023
5. Schmidt, P.: *Laserstrahlschweißen Elektrischer Kontakte von Lithium-Ionen-Batterien in Elektro- und Hybridfahrzeugen*. Doktorarbeit, Technische Universität, München (2015)
6. Grabmann, S., Kriegler, J., Harst, F., Günter, F.J., Zaeh, M.F.: Laser welding of current collector foil stacks in battery production—mechanical properties of joints welded with a green high-power disk laser. *Int. J. Adv. Manuf. Technol.* (2022). <https://doi.org/10.1007/s00170-021-07839-0>
7. Will, T., Müller, J., Müller, R., Hölbling, C., Goth, C., Schmidt, M.: Prediction of electrical resistance of laser-welded copper pin-pairs with surface topographical information from inline post-process observation by optical coherence tomography. *Int. J. Adv. Manuf. Technol.* (2023). <https://doi.org/10.1007/s00170-022-10796-x>
8. Engler, S.M.: *Laserstrahlschweißen von Kupferwerkstoffen mit brillanten Strahlquellen im infraroten und grünen Wellenlängenbereich*. Dissertation, Aachen, Technische Hochschule Aachen (2015)
9. Engler, S., Ramsayer, R., Poprawe, R.: Process studies on laser welding of copper with brilliant green and infrared lasers. *Phys. Procedia* (2011). <https://doi.org/10.1016/j.phpro.2011.03.142>
10. Kohl, S., Kaufmann, F., Schmidt, M.: Why color matters—proposing a quantitative stability criterion for laser beam processing of metals based on their fundamental optical properties. *Metals* (2022). <https://doi.org/10.3390/met12071118>
11. Franco, D.F.: *Wobbling laser beam welding of copper*. Dissertation, Universidade Nova de Lisboa (2017)
12. Helm, J., Schulz, A., Olowinsky, A., Dohrn, A., Poprawe, R.: Laser welding of laser-structured copper connectors for battery applications and power electronics. *Weld. World* (2020). <https://doi.org/10.1007/s40194-020-00849-8>
13. Poprawe, R.: *Tailored Light 2. Laser Application Technology*. RWTHedition. Springer Berlin Heidelberg, Berlin, Heidelberg (2011)
14. Franz, R., Wiedemann, G.: Ueber die Wärme-Leitungsfähigkeit der Metalle. *Ann. Phys. Chem.* (1853). <https://doi.org/10.1002/andp.18531650802>
15. Yaws, C.L.: *The Yaws Handbook of Physical Properties for Hydrocarbons and Chemicals. Physical Properties for more than 54,000 Organic and Inorganic Chemical Compounds, Coverage for C1 to C100 Organics and ac to zr Inorganics*. Elsevier Science GPP, Amsterdam [u.a.] (2015)
16. Mayer, G., Zähr, J., Füssel, U.: *Schweißen von Kupfer und Kupferlegierungen*. Deutsches Kupferinstitut (2009)
17. Lupp, F.: *Schweißen von Elektronikkomponenten mit grüner Laserstrahlung*. In: *Proceedings of LEF 2020*. Bayerisches Laserzentrum GmbH, Erlangen (2020)
18. Will, T., Kohl, J., Hoelbling, C., Müller, L., Schmidt, M.: Laser welding of different pure copper materials under consideration of shielding gas influence and impact on quality relevant surface topographical features. *J. Laser Appl.* (2023). <https://doi.org/10.2351/7.0000891>
19. Kaplan, A.F.H., Powell, J.: Spatter in laser welding. *J. Laser Appl.* (2011). <https://doi.org/10.2351/1.3597830>
20. Schulze, G.: *Die Metallurgie des Schweißens*, 3rd edn. Springer, Berlin (2004)
21. Rüttimann, C., Dürr, U., Moalem, A., Priehs, M.: Reliable laser micro-welding of copper. In: Gu, B., Hennig, G., Xu, X., Niino, H. (eds.) *Laser Applications in Microelectronic and Optoelectronic Manufacturing (LAMOM) XVI. SPIE LASE*, San Francisco, California, USA, Saturday 22 January 2011, p. 792007. SPIE (2011). <https://doi.org/10.1117/12.875033>
22. Weaver, J.H., Krafka, C., Lynch, D.W., Koch, E.E.: Optical properties of metals. *Appl. Opt.* (1981). https://doi.org/10.1364/AO.20.1124_1
23. Blom, A., Dunias, P., van Engen, P., Hoving, W., de Kramer, J.: Process spread reduction of laser microspot welding of thin copper parts using real-time control. In: *Photon Processing in Microelectronics and Photonics II*, pp. 493–507. International Society for Optics and Photonics (2003). <https://doi.org/10.1117/12.478612>

24. Kaufmann, F., Maier, A., Ermer, J., Roth, S., Schmidt, M.: Influence of defocusing in deep penetration welding of copper by using visible wavelength. In: Proceedings of the 11th International WLT-Conference on Lasers in Manufacturing. Wissenschaftlichen Gesellschaft Lasertechnik und Photonik e.V. (WLT), Munich (2021)
25. Graf, T., Berger, P., Weber, R., Hügel, H., Heider, A., Stritt, P.: Analytical expressions for the threshold of deep-penetration laser welding. *Laser Phys. Lett.* **12**, 56002 (2015)
26. Kaufmann, F., Forster, C., Hummel, M., Olowinsky, A., Beckmann, F., Moosmann, J., Roth, S., Schmidt, M.: Characterization of vapor capillary geometry in laser beam welding of copper with 515 nm and 1030 nm laser beam sources by means of in situ synchrotron X-ray imaging. *Metals* (2023). <https://doi.org/10.3390/met13010135>
27. Skupin, J.: Nichtlinear Dynamisches Modell zum Laserstrahlschweißen von Aluminiumlegierungen. Zugl.: Bremen, Univ., Diss., 2004. Berichte aus der Lasertechnik. Shaker, Aachen (2004)
28. Beck, M.: Modellierung des Lasertiefschweißens. Doctoral Thesis, Universität Stuttgart, Teubner Verlag, Stuttgart (1996)
29. Fabbro, R.: Basic processes in deep penetration laser welding. In: Beyer, E. (ed.) Congress Proceedings. ICALEO® 2002: 21st International Congress on Laser Materials Processing and Laser Microfabrication, Scottsdale, Arizona, USA, October 14–17, 2002, p. 380288. LIA, Orlando, Fla. (2002). <https://doi.org/10.2351/1.5065737>
30. Fabbro, R., Chouf, K.: Dynamical description of the keyhole in deep penetration laser welding. *J. Laser Appl.* (2000). <https://doi.org/10.2351/1.521924>
31. Fabbro, R., Chouf, K.: Keyhole modeling during laser welding. *J. Appl. Phys.* (2000). <https://doi.org/10.1063/1.373033>
32. Fabbro, R., Slimani, S., Coste, F., Briand, F.: Study of keyhole behaviour for full penetration Nd–Yag CW laser welding. *J Phys. D: Appl. Phys.* (2005). <https://doi.org/10.1088/0022-3727/38/12/005>
33. Reinheimer, E.N., Fetzter, F., Weber, R., Graf, T.: Benefit of high feed rates on the process efficiency in laser beam welding. *Procedia CIRP* (2020). <https://doi.org/10.1016/j.procir.2020.09.127>
34. Hügel, H., Graf, T.: *Laser in der Fertigung. Grundlagen der Strahlquellen, Systeme, Fertigungsverfahren*, 3rd edn. Lehrbuch. Springer Vieweg, Wiesbaden (2014)
35. Heider, A.: Erweitern der Prozessgrenzen beim Laserstrahlschweißen von Kupfer mit Einschweißiefen zwischen 1 mm und 10 mm. Dissertation, Universität Stuttgart, Herbert Utz Verlag, Munich (2018)
36. Heider, A., Weber, R., Herrmann, D., Herzog, P., Graf, T.: Power modulation to stabilize laser welding of copper. *J. Laser Appl.* (2015). <https://doi.org/10.2351/1.4906127>
37. Florian Oefe: Remote-Laserstrahlschweißen mit brillanten Laserstrahlquellen. Herbert Utz Verlag, Munich (2012)
38. Kawahito, Y., Wang, H.: In-situ observation of laser manufacturing with X-ray technique. *Synchrotron Radiation News* (2019). <https://doi.org/10.1080/08940886.2019.1582283>
39. Abt, F., Boley, M., Weber, R., Graf, T.: X-ray videography for investigation of capillary and melt pool dynamics in different materials. In: International Congress on Applications of Lasers & Electro-Optics. ICALEO® 2011: 30th International Congress on Laser Materials Processing, Laser Microprocessing and Nanomanufacturing, Orlando, Florida, USA, October 23–27, pp. 179–186. Laser Institute of America (2011). <https://doi.org/10.2351/1.5062233>
40. Heider, A., Sollinger, J., Abt, F., Boley, M., Weber, R., Graf, T.: High-speed X-Ray analysis of spatter formation in laser welding of copper. *Phys. Procedia* (2013). <https://doi.org/10.1016/j.phpro.2013.03.058>
41. Schrickler, K., Schmidt, L., Friedmann, H., Diegel, C., Seibold, M., Hellwig, P., Fröhlich, F., Bergmann, J.P., Nagel, F., Kallage, P., Rack, A., Requardt, H., Chen, Y.: Characterization of keyhole dynamics in laser welding of copper by means of high-speed synchrotron X-ray imaging. *Procedia CIRP* (2022). <https://doi.org/10.1016/j.procir.2022.08.079>
42. Hummel, M., Meier, C., Olowinsky, A., Gillner, A., Beckmann, F., Moosmann, J., Häfner, C.: In situ synchrotron observation of the vapor capillary geometry in laser welding of copper with 1030 nm and 515 nm laser beam sources. In: Kleine, K.R., Kaierle, S. (eds.) High-Power Laser Materials Processing: Applications, Diagnostics, and Systems XII. High-Power Laser Materials Processing: Applications, Diagnostics, and Systems XII, San Francisco, United States, 28.01.2023–03.02.2023, p. 19. SPIE (2023–2023). <https://doi.org/10.1117/12.2648946>
43. Lind, J., Fetzter, F., Blazquez-Sanchez, D., Weidensdorfer, J., Weber, R., Graf, T.: Geometry and absorptance of the cutting fronts during laser beam cutting. *J. Laser Appl.* (2020). <https://doi.org/10.2351/7.0000024>
44. Reinheimer, E., Hummel, M., Olowinsky, A., Weber, R., Graf, T.: High-speed synchrotron x-ray imaging of the formation of wedge-shaped capillaries during laser-beam welding at high feed rates.

- In: Proceedings of the Lasers in Manufacturing Conference 2021. Wissenschaftlichen Gesellschaft Lasertechnik und Photonik e.V. (WLT), Munich (2021)
45. Schaefer, M., Kessler, S., Fetzter, F., Graf, T.: Influence of the focal position on the melt flow during laser welding of steel. *J. Laser Appl.* (2017). <https://doi.org/10.2351/1.4972098>
 46. Tenner, F., Berg, B., Brock, C., Klämpfl, F., Schmidt, M.: Experimental approach for quantification of fluid dynamics in laser metal welding. *J. Laser Appl.* (2015). <https://doi.org/10.2351/1.4906302>
 47. Olfert, M., Bridger, P.M., Dunn, I., Duley, W.W.: Physical processes during laser drilling in the presence of a liquid. *High. Temp. Chem. Processes* **3**, 1–14 (1994)
 48. Agrawal, A.K., Rankouhi, B., Thoma, D.J.: Predictive process mapping for laser powder bed fusion: A review of existing analytical solutions. *Curr. Opin. Solid State Mater. Sci.* (2022). <https://doi.org/10.1016/j.cossms.2022.101024>
 49. Schell, N., King, A., Beckmann, F., Fischer, T., Müller, M., Schreyer, A.: The high energy materials science beamline (HEMS) at PETRA III. MSF (2013). <https://doi.org/10.4028/www.scientific.net/MSF.772.57>
 50. Weckert, E., Balewski, K., Brefeld, W., Decking, W., Drube, W.: PETRA III: A New High Brilliance Synchrotron Radiation Source at DESY. In: AIP Conference Proceedings. Synchrotron Radiation Instrumentation: Eighth International Conference on Synchrotron Radiation Instrumentation, San Francisco, California (USA), 25–29 August pp. 73–76. AIP (2003). <https://doi.org/10.1063/1.1757737>
 51. van der Veen, F., Pfeiffer, F.: Coherent x-ray scattering. *J. Phys.: Condens. Matter* (2004). <https://doi.org/10.1088/0953-8984/16/28/020>
 52. Harvey, A.C.: Forecasting, Structural time Series Model and Kalman Filter. Cambridge University Press, Cambridge, New York (1990)
 53. Press, W.H., Vetterling, W.T. (eds.): Numerical Recipes. The art of Scientific Computing, 3rd edn. Cambridge Univ. Press, Cambridge (2007)
 54. Oevel, W.: Einführung in die numerische Mathematik. Hochschultaschenbuch. Spektrum, Akad. Verl., Heidelberg, Berlin, Oxford (1996)
 55. Weberpals, J., Dausinger, F.: Influence of inclination angle on spatter behavior at welding with lasers of strong focusability. In: Congress Proceedings 2007. ICALEO®: 26th International Congress on Laser Materials Processing, Laser Microprocessing and Nanomanufacturing, Orlando, Florida, USA, October 29–November 1, 2007, p. 1602. Laser Institute of America, Orlando, Fla (2007). <https://doi.org/10.2351/1.5061015>
 56. berger, P., Hügel, H.: Fluid dynamic effects in keyhole welding – an attempt to characterize different regimes. *Phys. Procedia* (2013). <https://doi.org/10.1016/j.phpro.2013.03.072>
 57. Eriksson, I., Powell, J., Kaplan, A.: Melt behavior on the keyhole front during high speed laser welding. *Opt. Lasers Eng.* (2013). <https://doi.org/10.1016/j.optlaseng.2013.01.008>
 58. Dausinger, F.: Strahlwerkzeug Laser: Energieeinkopplung und Prozesseffektivität. Habilitationsschrift, Stuttgart (1995)
 59. Weberpals, J.-P.: Nutzen und Grenzen Guter Fokussierbarkeit beim Laserschweißen. Zugl.: Stuttgart, Univ., Diss., 2010. Laser in der Materialbearbeitung. Utz, München (2010)
 60. Reinheimer, E.N., Weber, R., Graf, T.: Influence of high feed rates during laser beam welding on the capillary geometry and the resulting weld seam quality. In: Kaieler, S. (ed.) High-Power Laser Materials Processing: Applications, Diagnostics, and Systems XI, San Francisco, United States, 1/22/2022–2/28/2022, p. 3. SPIE (2022). <https://doi.org/10.1117/12.2605540>
 61. Patschger, A., Seiler, M., Bliedtner, J.: Influencing factors on humping effect in laser welding with small aspect ratios. *J. Laser Appl.* (2018). <https://doi.org/10.2351/1.5040620>
 62. Miyagi, M., Zhang, X.: Investigation of laser welding phenomena of pure copper by x-ray observation system. *J. Laser Appl.* (2015). <https://doi.org/10.2351/1.4927609>
 63. Rykalin, N.N.: Berechnung der Wärmevergänge beim Schweißen. Verlag Technik, Berlin (1957)
 64. Kaplan, A.F.: Local flashing events at the keyhole front in laser welding. *Opt. Lasers Eng.* (2015). <https://doi.org/10.1016/j.optlaseng.2014.12.019>
 65. Reinheimer, E.N., Weber, R., Graf, T.: Influence of the capillary geometry on the weld seam quality during high-speed laser welding. *Procedia CIRP* (2022). <https://doi.org/10.1016/j.procir.2022.08.181>
 66. Fetzter, F., Hu, H., Berger, P., Weber, R., Graf, T.: Pores in laser beam welding: generation mechanism and impact on the melt flow. In: Kaieler, Heinemann (Hg.) – High-power Laser Materials Processing, p. 12. <https://doi.org/10.1117/12.2295798>
 67. Fetzter, F., Hagenlocher, C., Weber, R., Graf, T.: Geometry and stability of the capillary during deep-penetration laser welding of AlMgSi at high feed rates. *Opt. Laser Technol.* (2021). <https://doi.org/10.1016/j.optlastec.2020.106562>

Publisher's Note Springer Nature remains neutral with regard to jurisdictional claims in published maps and institutional affiliations.

Authors and Affiliations

Florian Kaufmann¹ · Julian Schrauder¹ · Marc Hummel^{2,3} · Christoph Spurk² · Alexander Olowinsky³ · Felix Beckmann⁴ · Julian Moosmann⁴ · Stephan Roth^{1,5} · Michael Schmidt^{1,5,6}

✉ Florian Kaufmann
f.kaufmann@blz.org

- ¹ Bayerisches Laserzentrum GmbH (blz), Konrad-Zuse-Str. 2-6, 91052 Erlangen, Germany
- ² Chair for Laser Technology LLT, RWTH Aachen University, Steinbachstr. 15, 52074 Aachen, Germany
- ³ Fraunhofer-Institut für Lasertechnik ILT, Steinbachstr. 15, 52074 Aachen, Germany
- ⁴ Institute of Materials Physics, Helmholtz-Zentrum Hereon, Max-Planck-Str. 1, 21502 Geesthacht, Germany
- ⁵ Erlangen Graduate School in Advanced Optical Technologies (SAOT), Paul-Gordan-Str. 6, 91052 Erlangen, Germany
- ⁶ Institute of Photonic Technologies (LPT), Friedrich-Alexander Universität Erlangen-Nürnberg, Konrad-Zuse-Str. 3/5, 91052 Erlangen, Germany